To cite this version :

J. PAUX, Mohamed BEN BETTAIEB, H. BADREDDINE, Farid ABED-MERAIM, C. LABERGERE, K. SAANOUNI - An elasto-plastic self-consistent model for damaged polycrystalline materials: Theoretical formulation and numerical implementation - Computer Methods in Applied Mechanics and Engineering - Vol. 368, p.113138 - 2020

An elasto-plastic self-consistent model for damaged polycrystalline materials: Theoretical formulation and numerical implementation

J. Paux[1,2,3], M. Ben Bettaieb[1,*], H. Badreddine[3], F. Abed-Meraim[1], C. Labergere[3], K. Saanouni[3]

[1]Arts et Metiers Institute of Technology, CNRS, Université de Lorraine, LEM3, F-57000, Metz, France

[2]IRT M2P, 4 rue Augustin Fresnel, F-57070 Metz, France

[3]ICD/LASMIS, University of Technology of Troyes, UMR 6281, CNRS, Troyes, France

Abstract

Elasto-plastic multiscale approaches are known to be suitable to model the mechanical behavior of metallic materials during forming processes. These approaches are classically adopted to explicitly link relevant microstructural effects to the macroscopic behavior. This paper presents a finite strain elasto-plastic self-consistent model for damaged polycrystalline aggregates and its implementation into ABAQUS/Standard finite element (FE) code. Material degradation is modeled by the introduction of a scalar damage variable at each crystallographic slip system for each individual grain. The single crystal plastic flow is described by both the classical and a regularized version of the Schmid criterion. To integrate the single crystal constitutive equations, two new numerical algorithms are developed (one for each plastic flow rule). Then, the proposed single crystal modeling is embedded into the self-consistent scheme to predict the mechanical behavior of elasto-plastic polycrystalline aggregates in the finite strain range. This strategy is implemented into ABAQUS/Standard FE code through a user-defined material (UMAT) subroutine. Special attention is paid to the satisfaction of the incremental objectivity and the efficiency of the convergence of the global resolution scheme, related to the computation of the consistent tangent modulus. The capability of the new constitutive modeling to capture the interaction between the damage evolution and the microstructural properties is highlighted through several simulations at both single crystal and polycrystalline scales. It appears from the numerical tests that the use of the classical Schmid criterion leads to a poor numerical convergence of the self-consistent scheme (due to the abrupt changes in the activity of the slip systems), which sometimes causes the computations to be prematurely stopped. By contrast, the use of the regularized version of the Schmid law allows a better convergence of the self-consistent approach, but induces an important increase in the computation

---

[*] Email address of the corresponding author: Mohamed.BenBettaieb@ensam.eu (M. Ben Bettaieb)

time devoted to the integration of the single crystal constitutive equations (because of the high value of the power-law exponent used to regularize the Schmid yield function). To avoid these difficulties, a numerical strategy is built to combine the benefits of the two approaches: the classical Schmid criterion is used to integrate the single crystal constitutive equations, while its regularized version is used to compute the microscopic tangent modulus required for solving the self-consistent equations. The robustness and the accuracy of this novel numerical strategy are particularly analyzed through several numerical simulations (prediction of the mechanical behavior of polycrystalline aggregates and simulation of a circular cup-drawing forming process).

Keywords: elasto-plasticity, finite strain, Schmid criterion, damaged single crystal, polycrystal, self-consistent scheme, numerical implementation, metal forming.

1. Introduction

In the field of material engineering, the modeling of the mechanical behavior in the finite strain range remains an active research topic. It is of prime importance in the optimization of forming process parameters and in the prediction of formability limits of metallic parts and components. Indeed, most forming processes, such as rolling or deep drawing, induce large plastic deformations, which lead to significant evolution of the material properties (hardening, plastic anisotropy, damage…). It is well known that crystallographic slip accommodates most of the plastic strains, while inducing plastic anisotropy in the mechanical response by evolution of crystallographic texture and dislocation structures. Additionally, the development of transgranular and intergranular mechanical fields plays a significant role in the deformation process, especially during unloading and reloading states [1]–[7]. Furthermore, nucleation, growth and coalescence of micro-voids and micro-cracks lead to the limitation of the formability of metallic components [8]–[9]. Hence, the evolution of macroscopic mechanical fields is governed by the evolution of the microstructural properties. These microstructural properties cannot be accurately modeled by the classical phenomenological approaches. To overcome this limitation and thus to accurately capture these properties, several multiscale schemes have been proposed. The aim of the present paper is to detail the numerical implementation of a new multiscale scheme involving damage at the grain scale. The current model ensures both the accuracy of the physical description and the robustness of the numerical computation. In this innovative model, three physical scales are taken into account: the single crystal scale, the polycrystal scale and the structural scale.

- **The single crystal scale:** in this contribution, a new single crystal constitutive model is developed. This model follows a finite strain rate-independent formulation, which is more suitable to model the evolution of the mechanical behavior during cold forming processes [10]–[13]. In this model, plastic strain is mainly due to the slip along the crystallographic slip systems (CSSs) and the plastic flow rule is modeled based on the classical Schmid criterion [14] and on one of its regularized versions [15]. This model allows taking into account the damage effects on the plastic

behavior using the concept of continuum damage mechanics (CDM), where a scalar damage variable is introduced at each CSS [16]–[17].

The numerical algorithms used to integrate the rate-independent single crystal constitutive equations based on the classical Schmid criterion (CSC) can be categorized in two main families: the return-mapping algorithms [18]–[21] and the ultimate algorithms [22]–[26]. Akpama et al. [27] have conducted an extensive comparative study on these two families of algorithms. It appears from this study that the class of ultimate algorithms is largely more efficient and more robust than the return-mapping algorithms. Consequently, the ultimate algorithm has been extended in the current work to integrate the damaged single crystal constitutive equations based on the classical Schmid criterion (called hereafter for brevity DCSC). The main tedious task in the numerical integration of these equations concerns the determination of the set of active CSSs and the corresponding slip rates. To achieve this task, the consistency condition, expressed based on the DCSC, could be mathematically formulated as a Non-Linear Complementarity Problem (NLCP). When damage is not considered, several numerical schemes have been developed to solve this complementarity problem. In this particular case, Ben Bettaieb et al. [26] have developed an implicit integration scheme to accurately solve the NLCP. More recently, Akpama et al. [27] have developed an explicit algorithm to solve the same problem after its linearization allowing the transformation of the NLCP into a linear complementarity problem (LCP). The robustness and the efficiency of this explicit algorithm, compared to the implicit one, for the integration of undamaged single crystal constitutive equations have been highlighted in [27]. In the present contribution, damage evolution is introduced in the constitutive equations, which requires some special care to be taken in the numerical integration of the constitutive equations. In fact, to consider the damage evolution, we have extended the explicit algorithm developed in [27]. In this case, the LCP is transformed into a quadratic complementarity problem (QCP), which is solved by the combinatorial search scheme [18], for the identification of the set of active CSSs, and by the fixed-point algorithm for the computation of the corresponding slip rates.

When the regularized Schmid criterion (RSC) is used for the modeling of the plastic flow, the problem of the determination of the set of active CSSs is obviously avoided and all the CSSs are simultaneously activated (in the elasto-plastic stage). In this case, the constitutive relations defining the expression of the slip rates are quite similar to those used in a viscoplastic formulation [28]. For viscoplastic single crystals, it is well known that the high value of the regularization exponent parameter leads to a very stiff non-linear problem. In such a situation, the computation of the slip rates experiences some convergence difficulties [29]. Several numerical techniques have been developed in the literature to circumvent these difficulties, such as the *k*-modification method proposed in [29]–[30] and the spectral database crystal plasticity approach developed in [31]–[33]. In the current investigation, the regularized Schmid criterion is extended to take into account the damage over the CSSs. The resulting model (denoted DRSC in what follows) is

integrated by developing a semi-implicit integration scheme based on the Newton–Raphson method. The developed scheme combines both accuracy and efficiency of the numerical integration.

To compare the predictions based on the two single crystal models (namely the DCSC and DRSC), several numerical simulations are presented in this paper. From these predictions, it turns out that the results obtained by the DRSC coincide with those obtained by DCSC when the regularization exponent parameter is sufficiently high (typically higher than 100). However, the computation time required to integrate the constitutive equations based on the DRSC is largely higher than that required by the DCSC.

- **The polycrystal scale:** the self-consistent approach is used in the current contribution to achieve the transition between the single crystal and polycrystal scales. Compared to the full-field multiscale approaches, such as the FE homogenization technique [34] or the FFT approach [35], the self-consistent scheme (mean-field approach) seems to be a good tradeoff to describe, accurately and efficiently, the mechanical behavior of polycrystalline materials. The higher performance of the self-consistent scheme in terms of computation time is even more evident when these approaches are embedded into a finite element strategy to simulate forming processes. In addition, the self-consistent approaches enable to overcome the limitations of the mean-field Taylor model. In fact, the application of the self-consistent scheme allows taking into account the equilibrium conditions in order to approach the strain localization at the grain level. Then, it allows more accurately describing the influence and the evolution of the texture morphology and the interaction between the grains and their surrounding ones. Numerically speaking, solving the self-consistent equations consists in the iterative computation of the macroscopic tangent modulus, which is based on the microscopic tangent moduli that relate the microscopic stress rate to its conjugate strain rate. Within the small strain framework, all of the strain and stress measures coincide, and there is no doubt on the choice of the conjugate mechanical variables. However, under finite strain conditions, there are various conjugate strain/stress measures, and choices are based on dissipation analysis. In the framework of Euler formulation, several authors have selected the Jaumann derivative of the Cauchy stress tensor and the Eulerian strain rate (the symmetric part of the velocity gradient) as conjugate variables to formulate the self-consistent equations [36]–[40]. This choice allows simplifying the numerical implementation of the self-consistent approach, which ensures easier convergence conditions for the iterative computations, but leads to some theoretical inconsistencies. Hill [41] suggested the use of the velocity gradient and the nominal stress rate in order to establish the transition relationship between microscopic and macroscopic stress and strain measures. Based on this choice, Lipinski and Berveiller [42] and Lipinski et al. [43] proposed a self-consistent approach to polycrystal plasticity at finite strains. Thanks to its sound theoretical basis, this formulation is adopted in the present work. This choice may also lead to some convergence difficulties when the DCSC is used. These difficulties

are mainly due to the continuous change in the set of active CSSs during loading. This problem has been early pointed out in [44]. This issue is naturally avoided when the Schmid criterion is regularized, as all CSSs are simultaneously activated in the plastic loading phase. Consequently, to ensure the efficiency and the convergence of the self-consistent scheme, the DCSC is adopted to integrate the microscopic constitutive equations, while the tangent modulus determined by the DRSC is used to achieve the self-consistent transition. This strategy, very similar to the numerical solution adopted in [44], allows combining the benefits of the two approaches. To carefully investigate the effect of the Schmid criterion regularization on the computation time and on the mechanical response of polycrystalline aggregates, several numerical predictions are carried out. These predictions reveal that the use of the mixed DCRSC (i.e., DCSC for the microscopic model and DRSC for the self-consistent computations) self-consistent approach allows us to obtain the same results as those given by the self-consistent scheme based on the DRSC, but with significantly reduced computation efforts.

- **The structural scale:** the different versions of the self-consistent approach (with the different combinations of plastic flow rules and numerical techniques) have been implemented as a user-defined material (UMAT) subroutine into ABAQUS/Standard FE code. In the present implementation, special attention is paid to the handling of the material rotation at the different scales and to the satisfaction of the incremental objectivity. The efficiency of the present constitutive modeling is assessed based on several numerical simulations.

This paper contains three main sections:

- The first one is devoted to the theoretical aspects of the developed constitutive model. The self-consistent equations are recalled. Then, the single crystal constitutive equations are presented with special focus on their coupling with ductile damage.

- The second part deals with the numerical and algorithmic aspects related to the model implementation at different scales. The specificities associated with the ABAQUS/Standard UMAT are also described.

- The third section is dedicated to numerical applications and presentation of the simulation results. First, basic tests on a single FE are presented to highlight the interaction between the various mechanical phenomena modeled. Then, structural computations are presented to assess the robustness of the implementation and the prediction capabilities of the model.

Conventions, notations and abbreviations

The following conventions and notations are adopted throughout this paper. Note that the assorted notations can be combined, while additional notations will be clarified as needed in the text:

- Microscale (resp. macroscale) variables are denoted by lowercase (resp. capital) letters.

- Vectors and tensors are indicated by **bold** letters or symbols. However, scalar parameters and variables are designated by thin and *italic* letters or symbols.

- Einstein's summation convention of implied summation over repeated indices is adopted. The range of free (resp. dummy) index is given before (resp. after) the corresponding equation.

- $\dot{\bullet}$ time derivative of $\bullet$.

- $\tilde{\bullet}$ the effective counterpart of the variable $\bullet$ (in the framework of damage mechanics).

- $\bullet^T$ transpose of $\bullet$.

- $\dot{\bullet}^C$ corotational derivative of $\bullet$.

- $\bullet^{-1}$ inverse of $\bullet$.

- $|\bullet|$ absolute value of $\bullet$.

- $\langle\bullet\rangle$ positive part of $\bullet$ or McCauley brackets.

- $e^\bullet$ exponential of $\bullet$.

- $\bullet.\bullet$ simple contraction or contraction on one index (inner product).

- $\bullet:\bullet$ double contraction or contraction on two indices (inner product).

- $\bullet\otimes\bullet$ tensorial product (external product).

- CSS   crystallographic slip system.

- CSC   model based on the classical Schmid criterion and the associated algorithm.

- RSC   model based on the regularized Schmid criterion and the associated algorithm.

- DCSC   model based on the damaged classical Schmid criterion and the associated algorithm.

- DRSC   model based on the damaged regularized Schmid criterion and the associated algorithm.

2. Constitutive framework

2.1. Polycrystal modeling

The mean-field self-consistent approach developed by Lipinski et al. [42]–[43] is used to model the mechanical behavior of polycrystalline aggregates starting from the behavior of their constituent grains (or crystal). In the self-consistent approach, each grain is assumed to be an ellipsoidal inclusion surrounded by a fictitious homogeneous and infinite medium that has the same properties as the polycrystal. As stated by Hill [41], within the framework of finite strains, the macroscopic Eulerian velocity gradient $\mathbf{G}$ and the macroscopic nominal stress rate $\dot{\mathbf{N}}$ should be selected as suitable strain

and stress measures to build the multiscale scheme. These macroscopic tensors are related to their microscopic counterparts $\mathbf{g}$ and $\dot{\mathbf{n}}$ by the Hill averaging theorem:

$$\mathbf{G} = \frac{1}{V}\int_V \mathbf{g}(\vec{\mathbf{x}})\mathrm{d}V \quad ; \quad \dot{\mathbf{N}} = \frac{1}{V}\int_V \dot{\mathbf{n}}(\vec{\mathbf{x}})\mathrm{d}V, \tag{1}$$

where $\vec{\mathbf{x}}$ is the vector of coordinates of a material point in the polycrystalline aggregate of volume V. The macroscopic nominal stress tensor $\mathbf{N}$ is related to the macroscopic Cauchy stress tensor $\boldsymbol{\Sigma}$ by the following relationship:

$$\mathbf{N} = J\ \mathbf{F}^{-1}\cdot\boldsymbol{\Sigma}, \tag{2}$$

with $\mathbf{F}$ the macroscopic deformation gradient and J its determinant.

By inversion of Eq. (1), the microscopic velocity gradient and nominal stress rate are linked to their macroscopic counterparts by the following relations:

$$\mathbf{g}(\vec{\mathbf{x}}) = \mathbf{A}(\vec{\mathbf{x}}):\mathbf{G} \quad ; \quad \dot{\mathbf{n}}(\vec{\mathbf{x}}) = \mathbf{B}(\vec{\mathbf{x}}):\dot{\mathbf{N}}, \tag{3}$$

where $\mathbf{A}(\vec{\mathbf{x}})$ and $\mathbf{B}(\vec{\mathbf{x}})$ are fourth-rank concentration tensors for the velocity gradient and the nominal stress rate, respectively.

The self-consistent approach allows linking $\dot{\mathbf{N}}$ to $\mathbf{G}$ through the macroscopic fourth-rank tangent modulus $\mathcal{L}$:

$$\dot{\mathbf{N}} = \mathcal{L}:\mathbf{G}. \tag{4}$$

At the microscopic level, a relationship similar to Eq. (4) can be derived by combining the constitutive relations of the single crystal:

$$\dot{\mathbf{n}}(\vec{\mathbf{x}}) = \boldsymbol{\ell}(\vec{\mathbf{x}}):\mathbf{g}(\vec{\mathbf{x}}), \tag{5}$$

where $\boldsymbol{\ell}$ is the microscopic fourth-rank tangent modulus. The relation between $\mathcal{L}$ and $\boldsymbol{\ell}$ can be obtained by combining Eqs. (4)–(5):

$$\mathcal{L} = \frac{1}{V}\int_V \boldsymbol{\ell}(\vec{\mathbf{x}}):\mathbf{A}(\vec{\mathbf{x}})\mathrm{d}V. \tag{6}$$

Furthermore, it is assumed that all mechanical variables are homogeneous within each individual single crystal. Thus, for any grain gr, Eqs. (3)$_1$ and (5) become:

$$\mathbf{g}^{gr} = \mathbf{A}^{gr}:\mathbf{G} \quad ; \quad \dot{\mathbf{n}}^{gr} = \boldsymbol{\ell}^{gr}:\mathbf{g}^{gr}. \tag{7}$$

By using Green's tensor and some classical mathematical developments [45], an approximate version of the concentration tensor $\mathbf{A}^{gr}$ is given by the following expression:

$$\mathbf{A}^{gr} = \left(\mathbf{I}_4 - \mathbf{T}^{gr}:\left(\boldsymbol{\ell}^{gr}-\mathcal{L}\right)\right)^{-1}:\left(\sum_{gr=1}^{Ngr}f^{gr}\ \left(\mathbf{I}_4 - \mathbf{T}^{gr}:\left(\boldsymbol{\ell}^{gr}-\mathcal{L}\right)\right)^{-1}\right)^{-1}, \tag{8}$$

where $\mathbf{I}_4$ is the fourth-rank identity tensor, $\mathbf{T}^{gr}$ is a fourth-rank tensor describing the interaction between grain gr and its surrounding ones, and Ngr is the total number of grains within the polycrystalline aggregate. Tensor $\mathbf{T}^{gr}$ is mainly dependent on $\mathcal{L}$ and its explicit analytical expression can only be found for isotropic elastic solids. For the proposed finite strain model, which involves strong textural and morphological anisotropy induced by the plastic strain and lattice spin, the interaction tensor $\mathbf{T}^{gr}$ is computed based on Fourier's transforms [45]–[46] through an integral over an ellipsoid representing the grain gr. The macroscopic tangent modulus derived by the 1-site self-consistent version of the incremental scheme of Hill [41] is finally obtained as follows:

$$\mathcal{L} = \sum_{gr=1}^{Ngr} f^{gr} \, \boldsymbol{\ell}^{gr} : \mathbf{A}^{gr}, \tag{9}$$

where f^{gr} is the volume fraction of the grains having the same crystallographic orientation.

2.2. Single crystal modeling

The single crystal constitutive modeling can be classically expressed in the form of Eq. (7). To reach this form, the single crystal kinematics are briefly revisited in Section 2.2.1. Then, the elastic part of mechanical behavior is formulated in Section 2.2.2. After that, the rules used to model the single crystal plastic flow are detailed in Section 2.2.3. Finally, the analytical expression of the microscopic tangent modulus ℓ is derived in Section 2.2.4.

2.2.1. Single crystal kinematics

The kinematics equations of finite strain crystal plasticity, leading to the additive decomposition of the microscopic velocity gradient $\mathbf{g}$ into elastic and plastic parts, are provided in Appendix A. These kinematics equations are required to clearly present the single crystal constitutive framework based on the assumption that the plastic strain is uniquely due to the slip on N_s CSSs. Each CSS k is defined, in the deformed configuration, by two vectors $\vec{\mathbf{m}}^k$ and $\vec{\mathbf{n}}^k$ standing for the slip direction and the normal to the slip plane, respectively (Fig. A.1). The symmetric and skew-symmetric parts of the tensor product $\vec{\mathbf{m}}^k \otimes \vec{\mathbf{n}}^k$ (which is known as the Schmid orientation tensor for CSS k) are denoted by $\boldsymbol{\mu}^k$ and $\mathbf{s}^k$, respectively. In the intermediate configuration related to the crystallographic lattice defined by rotation $\mathbf{r}^e$ (Fig. A.1), the counterparts of $\vec{\mathbf{m}}^k$ and $\vec{\mathbf{n}}^k$ remain fixed throughout the deformation. In most single crystal models, it has been assumed that the contribution of CSS k to the single crystal plastic deformation is coaxial to the Schmid tensor $\boldsymbol{\mu}^k$. But sometimes, this coaxiality property is not fulfilled, as crystallographic slip on this system may induce other phenomena, such as crack propagation leading to plastic deformation not coaxial to $\boldsymbol{\mu}^k$ [16]. To take into account this effect, a second-rank tensor $\widehat{\boldsymbol{\mu}}^k$ is introduced, which describes the deviation of the plastic strain from the Schmid tensor. The explicit

expression of tensor $\hat{\boldsymbol{\mu}}^k$, along with further developments, will be given in Section 2.3. As a result, tensors $\mathbf{d}^p$ and $\mathbf{w}^p$ can be expressed as:

$$\begin{cases} \mathbf{d}^p = \dot{\gamma}^k \left(\boldsymbol{\mu}^k + \hat{\boldsymbol{\mu}}^k \right) \\ \mathbf{w}^p = \dot{\gamma}^k \, \mathbf{s}^k \end{cases} \quad ; \quad k = 1, ..., N_s, \tag{10}$$

where the plastic spin $\mathbf{w}^p$ characterizes the evolution of the difference between the rotation rate $\dot{\mathbf{r}} = \mathbf{w} \cdot \mathbf{r}$ of the current configuration and the rotation rate $\dot{\mathbf{r}}^e = \mathbf{w}^e \cdot \mathbf{r}^e$ of the single crystal lattice (the intermediate configuration) with respect to the initial configuration. The different configurations (namely, initial, intermediate and current configurations) are schematically illustrated in Fig. A.1. For practical reasons, and for handling only positive values of slip rates in the subsequent theoretical and numerical developments, it is more convenient to split each CSS into two opposite oriented CSSs $\left(\vec{\mathbf{m}}^k, \vec{\mathbf{n}}^k \right)$ and $\left(-\vec{\mathbf{m}}^k, \vec{\mathbf{n}}^k \right)$, numbered k and $k + N_s$, respectively. With this decomposition, Eq. (10) is transformed into the following form [27]:

$$\begin{cases} \mathbf{d}^p = \dot{\gamma}^k \left(\boldsymbol{\mu}^k + \hat{\boldsymbol{\mu}}^k \right) \\ \mathbf{w}^p = \dot{\gamma}^k \, \mathbf{s}^k \end{cases} \quad \text{with} \quad \dot{\gamma}^k \geq 0; \quad k = 1, ..., 2N_s. \tag{11}$$

2.2.2. Single crystal elastic model

The effect of damage evolution on the single crystal behavior is thoroughly considered in the current model. Damage is assumed to affect both elastic and plastic properties. To satisfy the objectivity principle, the lattice corotational derivatives $\dot{\boldsymbol{\sigma}}^c$ of the Cauchy stress tensor $\boldsymbol{\sigma}$ is related to the elastic strain rate by the following damaged hypoelastic model [17]:

$$\dot{\boldsymbol{\sigma}}^c = \dot{\boldsymbol{\sigma}} - \mathbf{w}^e.\boldsymbol{\sigma} + \boldsymbol{\sigma}.\mathbf{w}^e = \tilde{\mathbf{c}}^e : \mathbf{d}^e + \dot{\tilde{\mathbf{c}}}^e : \boldsymbol{\varepsilon}^e, \tag{12}$$

where $\boldsymbol{\varepsilon}^e$ is the integral of the elastic strain rate $\mathbf{d}^e$ over the loading history in the lattice corotational frame, and $\tilde{\mathbf{c}}^e$ is the elasticity modulus for the damaged materiel, which is related to its counterpart for undamaged materiel $\mathbf{c}^e$ by the following classical relation [47]:

$$\tilde{\mathbf{c}}^e = \left(1 - d_{av} \right) \mathbf{c}^e. \tag{13}$$

The scalar damage variable d_{av} describes the effect of micro-damage on the elastic properties and its evolution equation will be given later in Eq. (28). In the present work, the elasticity of the undamaged material is assumed to be infinitesimal, linear and isotropic. Hence, matrix $\mathbf{c}^e$ only depends on the Young modulus E and the Poisson ratio ν.

2.2.3. Single crystal plastic flow rules

Two versions of the Schmid flow rule have been extended to take into account the effect of damage on the single crystal plastic behavior: the classical Schmid rule and the regularized version developed by

Gambin and Barlat [15]. For the sake of brevity, the formulated extended flow rules will be called in what follows DCSC (damaged classical Schmid criterion) and DRSC (damaged regularized Schmid criterion).

2.2.3.1. DCSC

To define the damaged classical Schmid criterion, let us introduce the resolved shear stress, which is defined as the projection of the Cauchy stress tensor $\boldsymbol{\sigma}$ on the Schmid tensor of CSS k :

$$\forall k = 1,...,2N_s: \quad \tau^k = \boldsymbol{\sigma}:\boldsymbol{\mu}^k, \tag{14}$$

and the critical shear stress τ_c^k defining the limit of the single crystal yield locus. The evolution of τ_c^k is described by the following generic hardening rule:

$$\forall k = 1,...,2N_s: \quad \dot{\tau}_c^k = h^{kl}\dot{\gamma}^l \quad ; \quad l = 1,...,2N_s, \tag{15}$$

where $\mathbf{h}$ is an interaction hardening matrix. The components of this matrix are generally variable and depend on the accumulated slip on the different CSSs.

To consider the ductile damage effect on the plastic behavior, a damage variable d^k is introduced for each CSS. Thus, the 'actual' resolved shear stress τ^k and slip rate $\dot{\gamma}^k$ are linked to their effective counterparts $\tilde{\tau}^k$ and $\dot{\tilde{\gamma}}^k$ by the following relations, based on the energy equivalence assumption [16]:

$$\forall k = 1,...,2N_s: \quad \tilde{\tau}^k = \frac{\tau^k}{\sqrt{1-d^k}} \quad ; \quad \dot{\tilde{\gamma}}^k = \sqrt{1-d^k}\,\dot{\gamma}^k. \tag{16}$$

By using the effective variables, the classical Schmid criterion can be extended to take into account the effect of damage evolution on the plastic flow [16]:

$$\forall k = 1,...,2N_s: \quad \tilde{f}^k = \tilde{\tau}^k + \alpha\tilde{\sigma}_\eta^k\sum_{r=1}^{2N_s}d^r - \tau_c^k \le 0 \quad ; \quad \dot{\tilde{\gamma}}^k \ge 0 \quad ; \quad \dot{\tilde{\gamma}}^k\,\tilde{f}^k = 0, \tag{17}$$

where $\tilde{f}^k$ is the effective yield function corresponding to CSS k, α is a material parameter related to the damage-induced softening phenomenon, and $\tilde{\sigma}_\eta^k$ is an effective crack-opening stress, normal to the slip plane k, defined by the following relations:

$$\forall k = 1,...,2N_s: \quad \tilde{\sigma}_\eta^k = \frac{\sigma_\eta^k}{\sqrt{1-d^k}} \quad \text{and} \quad \sigma_\eta^k = \left\langle \boldsymbol{\sigma}:\boldsymbol{\eta}^k \right\rangle. \tag{18}$$

In Eq. (18), $\boldsymbol{\eta}^k$ is a second-rank tensor corresponding to the opening of the micro-cracks in the slip plane $\mathbf{n}^k$, which is defined as follows:

$$\forall k = 1,...,2N_s: \quad \boldsymbol{\eta}^k = \vec{\mathbf{n}}^k \otimes \vec{\mathbf{n}}^k = \boldsymbol{\eta}_h^k + \boldsymbol{\eta}_{dev}^k, \tag{19}$$

where $\boldsymbol{\eta}_h^k$ (resp. $\boldsymbol{\eta}_{dev}^k$) is the hydrostatic (resp. deviatoric) part of tensor $\boldsymbol{\eta}^k$. Equation (18) states that the slip system resistance weakens when $\boldsymbol{\sigma}:\boldsymbol{\eta}^k > 0$, which corresponds to micro-crack opening, while this resistance remains unchanged when $\boldsymbol{\sigma}:\boldsymbol{\eta}^k \leq 0$. A schematic illustration of the physical influence of tensor $\boldsymbol{\eta}^k$ is depicted in Fig. 1. As will be shown hereafter, the presence of the hydrostatic component $\boldsymbol{\eta}_h^k$ induces plastic compressibility [48].
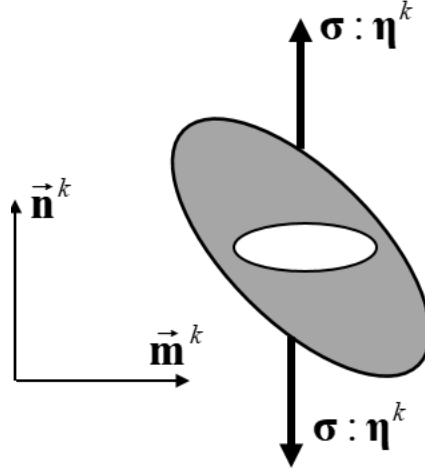

Fig. 1. Schematic illustration of the influence of microcracks opening on the resistance of a typical slip system.

As for the case of the classical model, the yield locus corresponding to the damaged classical Schmid criterion (DCSC) given by Eq. (17) is a non-smooth surface, which is defined by the intersection of multiple planes (see Fig. 2).

It is worth noting that, without micro-cracks (i.e., when $d^k = 0$ for all CSSs), the crack-opening stress σ_η^k does not enter the expression of the flow rule (see Eq. (17)) and, hence, has no influence on it. However, when damage is considered in the modeling, σ_η^k induces some dependence of the plastic flow on the hydrostatic stress, which is known to affect the metal failure. For simplicity of the upcoming developments, let us introduce the slip variables $\widehat{\tilde{\tau}}^k$ and $\widehat{\boldsymbol{\mu}}_c^k$ defined as:

$$\forall k = 1,...,2\,N_s: \quad \widehat{\tilde{\tau}}^k = \tilde{\tau}^k + \alpha \tilde{\sigma}_\eta^k \sum_{r=1}^{2N_s} d^r \quad ; \quad \widehat{\boldsymbol{\mu}}_c^k = \boldsymbol{\mu}^k + \alpha\, s^k \boldsymbol{\eta}^k \sum_{r=1}^{2N_s} d^r \quad \text{with} \quad s^k = \begin{cases} 0 & \text{if} \quad \sigma_\eta^k = 0 \\ 1 & \text{otherwise} \end{cases}.$$

(20)

Considering the above definition of $\widehat{\tilde{\tau}}^k$ and $\widehat{\boldsymbol{\mu}}_c^k$, the effective yield function $\tilde{f}^k$ can be rewritten as:

$$\forall k = 1,...,2\,N_s: \quad \tilde{f}^k = \widehat{\tilde{\tau}}^k - \tau_c^k = \frac{\boldsymbol{\sigma}:\widehat{\boldsymbol{\mu}}_c^k}{\sqrt{1-d^k}} - \tau_c^k.$$

(21)

In the meanwhile, the plastic deformation induces propagation of micro-cracks, and thus a normal deformation component, due to the surface tension of the micro-cracks. Considering this phenomenon, a normal strain term is added to the plastic strain:

$$\mathbf{d}^P = \dot{\gamma}^k (\boldsymbol{\mu}^k + \alpha\,\boldsymbol{\eta}^k \sum_{r=1}^{2N_s} d^r) \quad ; \quad k = 1, ..., 2N_s. \tag{22}$$

By comparing Eqs. (11)$_1$ and (22), the expression of tensor $\widehat{\boldsymbol{\mu}}^k$ can be identified:

$$\forall k = 1, ..., 2N_s: \quad \widehat{\boldsymbol{\mu}}^k = \alpha\,\boldsymbol{\eta}^k \sum_{r=1}^{2N_s} d^r. \tag{23}$$

As for the yield function $\tilde{f}^k$, one defines the equivalent Schmid tensor corresponding to the plastic strain as:

$$\forall k = 1, ..., 2\,N_s: \quad \widehat{\boldsymbol{\mu}}_{\mathbf{d}^P}^k = \boldsymbol{\mu}^k + \alpha\,\boldsymbol{\eta}^k \sum_{r=1}^{2N_s} d^r. \tag{24}$$

The insertion of Eq. (24) into Eq. (22) allows us to give the following expression to $\mathbf{d}^P$:

$$\mathbf{d}^P = \frac{\dot{\tilde{\gamma}}^k}{\sqrt{1 - d^k}} \widehat{\boldsymbol{\mu}}_{\mathbf{d}^P}^k \quad ; \quad k = 1, ..., 2N_s. \tag{25}$$

Hence, plastic strain has a hydrostatic component leading to an induced volume variation, or compressibility induced by the term controlled by the micro-crack opening (see Eq. (19)). Moreover, the plastic behavior is no longer associative. Indeed, plastic associativity would have implied that:

$$\mathbf{d}^P = \dot{\tilde{\gamma}}^k \frac{\partial \tilde{f}^k}{\partial \boldsymbol{\sigma}} = \frac{\dot{\tilde{\gamma}}^k}{\sqrt{1 - d^k}} \widehat{\boldsymbol{\mu}}_c^k \quad ; \quad k = 1, ..., 2N_s, \tag{26}$$

which is not always verified, as $\widehat{\boldsymbol{\mu}}_{\mathbf{d}^P}^k \neq \widehat{\boldsymbol{\mu}}_c^k$ when $\sigma_\eta^k > 0$ (which corresponds to a tension state). A relevant thermodynamically-consistent formulation has been established by Saanouni et al. [17] to ensure the physical consistency of this plasticity flow rule. In practice, this non-associativity induces a difference between tension and compression states, which is consistent with crack-propagation framework.

The above equations are complemented by the evolution equation of the ductile damage variable d^k. In the current contribution, the model developed by Saanouni et al. [17] is adopted:

$$\forall k = 1, ..., N_s: \quad \dot{d}^k = \dot{d}^{k+N_s} = \left(\dot{\tilde{\gamma}}^k + \dot{\tilde{\gamma}}^{k+N_s}\right) \left(\frac{Y^k - Y^0}{S}\right)^\beta \frac{1}{(1 - d^k)^m} := \left(\dot{\tilde{\gamma}}^k + \dot{\tilde{\gamma}}^{k+N_s}\right) v^k. \tag{27}$$

This evolution equation depends on the thermodynamic force Y^k, associated with the damage variable d^k, and on the following material parameters: Y^0, S, β and m.

The evolution equation of the averaged damage variable d_{av}, introduced in Eq. (13), is related to the rate of the slip damage variables d^k by:

$$\dot{d}_{av} = \frac{1}{2N_s} \sum_{k=1}^{2N_s} \dot{d}^k .$$

(28)

Since

$$\forall\, k = 1,...,N_s: \quad v^k = v^{k+N_s} ,$$

(29)

equation (28) can be reformulated as:

$$\dot{d}_{av} = \frac{1}{2N_s} \sum_{k=1}^{2N_s} \dot{d}^k = \frac{1}{2N_s}\left(\sum_{k=1}^{N_s}\left(\dot{\tilde{\gamma}}^k + \dot{\tilde{\gamma}}^{k+N_s}\right) v^k + \sum_{k=1+N_s}^{2N_s}\left(\dot{\tilde{\gamma}}^k + \dot{\tilde{\gamma}}^{k-N_s}\right) v^k \right) = \frac{1}{N_s} \sum_{k=1}^{2N_s} \dot{\tilde{\gamma}}^k v^k .$$

(30)

2.2.3.2. DRSC

A regularized form of the Schmid criterion (RSC) has been developed by Gambin and Barlat [15]. Contrary to the CSC defined by a non-smooth yield locus, the regularization of the Schmid criterion allows smoothing the corresponding yield function (see Fig. 2). The RSC is extended in the current investigation to integrate the damage effects. The yield function corresponding to this regularized version reads:

$$\tilde{f}_{reg} = \sum_{k=1}^{N_s}\left(\frac{\tilde{\tau}^k}{\tau_c^k}\right)^{2n} - 1 \le 0 ,$$

(31)

where n is a positive integer acting as a regularization parameter. When parameter n goes to infinity, the regularized yield function given by Eq. (31) tends to the classical yield function, as illustrated in Fig. 2.
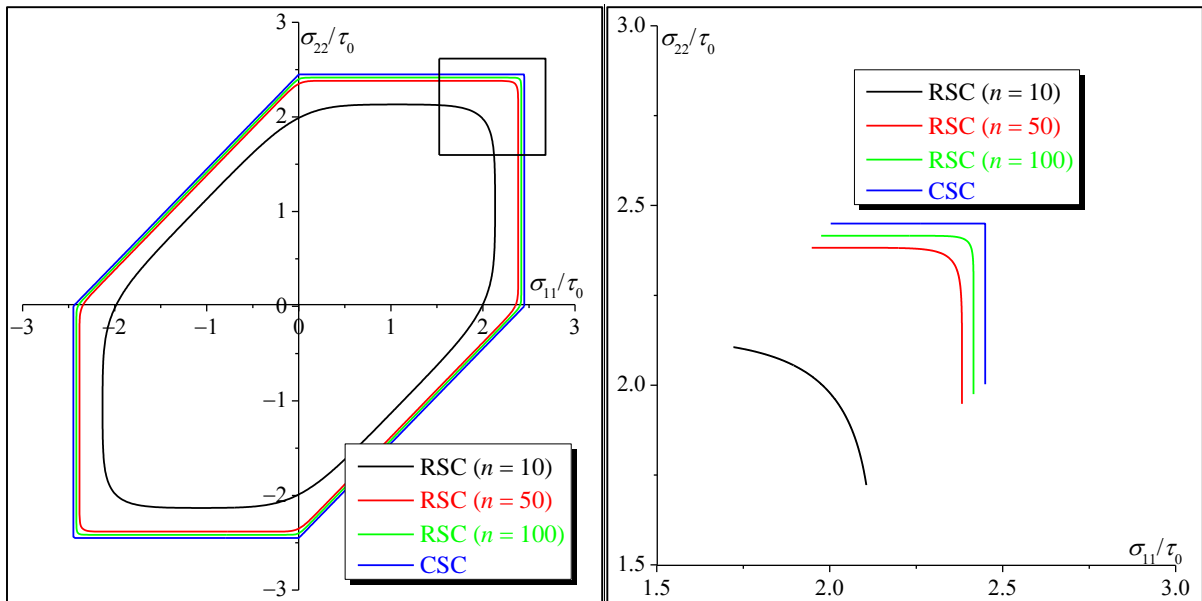
Fig. 2. Effect of the regularization parameter n on the shape of FCC single crystal yield locus: (a) Complete yield loci; (b) zoom on the corner zone.

In the same spirit as the DCSC, the plastic strain rate $\mathbf{d}^p$ derived from the DRSC can be defined as follows:

$$\mathbf{d}^p = 2\,\dot{\lambda}\,n\sum_{k=1}^{N_s}\left(\frac{\widehat{\widetilde{\tau}}^{\,k}}{\tau_c^k}\right)^{2n-1}\frac{\widehat{\boldsymbol{\mu}}_{\mathbf{d}^p}^k}{\sqrt{1-d^k\,\tau_c^k}}, \tag{32}$$

where $\dot{\lambda}$ is the plastic multiplier.

It must be noted that, as for the DCSC, the normality rule is not fulfilled here as:

$$\mathbf{d}^p \neq \dot{\lambda}\frac{\partial\,\tilde{f}_{reg}}{\partial\boldsymbol{\sigma}} = 2\,\dot{\lambda}\,n\sum_{k=1}^{N_s}\left(\frac{\widehat{\widetilde{\tau}}^{\,k}}{\tau_c^k}\right)^{2n-1}\frac{\widehat{\boldsymbol{\mu}}_c^k}{\sqrt{1-d^k\,\tau_c^k}}. \tag{33}$$

The flow rule for the DRSC can be defined by the following two inequalities and equality (equivalent to Eq. (20) for the DCSC):

$$\dot{\lambda} \geq 0 \quad ; \quad \tilde{f}_{reg} \leq 0 \quad ; \quad \dot{\lambda}\,\tilde{f}_{reg} = 0. \tag{34}$$

The expression of the slip rates for the different CSSs can be identified from Eq. (32):

$$\forall\,k=1,...,N_s: \quad \dot{\tilde{\gamma}}^k = \dot{\lambda}\left\langle\frac{2\,n}{\tau_c^k}\left(\frac{\widehat{\widetilde{\tau}}^{\,k}}{\tau_c^k}\right)^{2n-1}\right\rangle := \dot{\lambda}\,\kappa^k; \quad \dot{\tilde{\gamma}}^{k+N_s} = \dot{\lambda}\left\langle-\frac{2\,n}{\tau_c^k}\left(\frac{\widehat{\widetilde{\tau}}^{\,k}}{\tau_c^k}\right)^{2n-1}\right\rangle := \dot{\lambda}\,\kappa^{k+N_s}, \tag{35}$$

where κ^k is a slip variable defined to simplify the subsequent developments.

2.2.4. Computation of the single crystal tangent modulus

A general expression for the microscopic tangent modulus ℓ, valid for both DCSC and DRSC, is derived in the current section. As stated by Eq. (7), this tangent modulus allows us to relate the nominal stress rate $\dot{\mathbf{n}}$ to the velocity gradient $\mathbf{g}$. The microscopic nominal stress $\mathbf{n}$ is related to the microscopic Cauchy stress $\boldsymbol{\sigma}$ by the microscopic counterpart of Eq. (2):

$$\mathbf{n} = j\,\mathbf{f}^{-1}\cdot\boldsymbol{\sigma}. \tag{36}$$

Time derivation of equation (36) allows obtaining, after some mathematical developments detailed in [42], the following expression for the nominal stress rate $\dot{\mathbf{n}}$:

$$\dot{\mathbf{n}} = j\,\mathbf{f}^{-1}.\left(\dot{\boldsymbol{\sigma}} + tr(\mathbf{g})\boldsymbol{\sigma} - \mathbf{g}.\boldsymbol{\sigma}\right), \tag{37}$$

where j is the determinant of the microscopic deformation gradient $\mathbf{f}$. By adopting an updated Lagrangian approach (i.e., $j=1$ and $\mathbf{f}=\mathbf{I}_2$), Eq. (37) reduces to the following form:

$$\dot{\mathbf{n}} = \dot{\boldsymbol{\sigma}} + tr(\mathbf{g})\boldsymbol{\sigma} - \mathbf{g}.\boldsymbol{\sigma} = \dot{\boldsymbol{\sigma}} + \boldsymbol{\ell}^1 : \mathbf{g}, \tag{38}$$

where the fourth-rank tensor $\boldsymbol{\ell}^1$ is given by the following index form:

$$\ell^1_{ijkl} = \delta_{kl}\sigma_{ij} - \delta_{ki}\sigma_{lj}. \tag{39}$$

The expression of the Cauchy stress rate $\dot{\boldsymbol{\sigma}}$, required in Eq. (38) to compute $\dot{\mathbf{n}}$, is obtained by combining Eqs. (A.7) and (12):

$$\dot{\boldsymbol{\sigma}} = \tilde{\mathbf{c}}^e : (\mathbf{d} - \mathbf{d}^p) + \dot{\tilde{\mathbf{c}}}^e : \boldsymbol{\varepsilon}^e + (\mathbf{w} - \mathbf{w}^p).\boldsymbol{\sigma} - \boldsymbol{\sigma}.(\mathbf{w} - \mathbf{w}^p)$$
$$= \boldsymbol{\ell}^2 : \mathbf{g} + \tilde{\mathbf{c}}^e : \mathbf{d} + \dot{\tilde{\mathbf{c}}}^e : \boldsymbol{\varepsilon}^e - \tilde{\mathbf{c}}^e : \mathbf{d}^p + \boldsymbol{\sigma}.\mathbf{w}^p - \mathbf{w}^p.\boldsymbol{\sigma}, \tag{40}$$

where $\boldsymbol{\ell}^2$ is a fourth-rank tensor defined by the following index form:

$$\ell^2_{ijkl} = \frac{1}{2}\left(\delta_{ki}\sigma_{lj} - \delta_{il}\sigma_{kj} - \delta_{lj}\sigma_{ik} + \delta_{jk}\sigma_{il}\right). \tag{41}$$

On the other hand, $\dot{\tilde{\mathbf{c}}}^e$ can be determined by combining Eqs. (13) and (30):

$$\dot{\tilde{\mathbf{c}}}^e = -\dot{d}_{av}\,\mathbf{c}^e = -\frac{1}{N_s}\dot{\gamma}^l v^l \mathbf{c}^e \quad ; \quad l = 1,\dots,2N_s. \tag{42}$$

By using expression (42) for $\dot{\tilde{\mathbf{c}}}^e$ and Eqs. (11)$_2$ and (22) defining $\mathbf{w}^p$ and $\mathbf{d}^p$, one can deduce the following expression of $\dot{\boldsymbol{\sigma}}$:

$$\dot{\boldsymbol{\sigma}} = \boldsymbol{\ell}^2 : \mathbf{g} + \tilde{\mathbf{c}}^e : \mathbf{d} - \sum_{k=1}^{2N_s}\dot{\gamma}^k\left(\frac{1}{N_s}v^k\mathbf{c}^e : \boldsymbol{\varepsilon}^e + \frac{\tilde{\mathbf{c}}^e : \hat{\boldsymbol{\mu}}^k_{\mathbf{d}^p} - \boldsymbol{\sigma}.\mathbf{s}^k + \mathbf{s}^k.\boldsymbol{\sigma}}{\sqrt{1-d^k}}\right), \tag{43}$$

which can be rewritten as:

$$\dot{\boldsymbol{\sigma}} = \boldsymbol{\ell}^2 : \mathbf{g} + \tilde{\mathbf{c}}^e : \mathbf{d} - \sum_{k=1}^{2N_s}\left(\mathbf{Y}^k : \mathbf{g}\right)\left(\frac{1}{N_s}v^k\mathbf{c}^e : \boldsymbol{\varepsilon}^e + \frac{\tilde{\mathbf{c}}^e : \hat{\boldsymbol{\mu}}^k_{\mathbf{d}^p} - \boldsymbol{\sigma}.\mathbf{s}^k + \mathbf{s}^k.\boldsymbol{\sigma}}{\sqrt{1-d^k}}\right), \tag{44}$$

where $\mathbf{Y}^k$ is a second-rank tensor linking the slip rate $\dot{\gamma}^k$ to the microscopic Eulerian velocity gradient $\mathbf{g}$:

$$\dot{\gamma}^k = \mathbf{Y}^k : \mathbf{g}. \tag{45}$$

Then, combining Eqs. (7), (38) and (44), the expression of the single crystal tangent modulus $\boldsymbol{\ell}$ can be given in the following form:

$$\boldsymbol{\ell} = \boldsymbol{\ell}^1 + \boldsymbol{\ell}^2 + \tilde{\mathbf{c}}^e - \sum_{k=1}^{2N_s}\left(\frac{1}{N_s}v^k\mathbf{c}^e : \boldsymbol{\varepsilon}^e + \frac{\tilde{\mathbf{c}}^e : \hat{\boldsymbol{\mu}}^k_{\mathbf{d}^p} - \boldsymbol{\sigma}.\mathbf{s}^k + \mathbf{s}^k.\boldsymbol{\sigma}}{\sqrt{1-d^k}}\right) \otimes \mathbf{Y}^k. \tag{46}$$

The expression of tensors $\mathbf{Y}^k$ depends on the adopted plastic flow rule (DCSC or DRSC). The detailed expression of tensors $\mathbf{Y}^k$ for both flow rules is derived in Appendix B. When damage evolution is not

considered in the constitutive modeling, expression (46) of the elasto-plastic tangent modulus reduces to the following form:

$$\boldsymbol{\ell} = \boldsymbol{\ell}^1 + \boldsymbol{\ell}^2 + \mathbf{c}^e - \sum_{k=1}^{2N_s} \left(\mathbf{c}^e : \boldsymbol{\mu}^k - \boldsymbol{\sigma}.\mathbf{s}^k + \mathbf{s}^k.\boldsymbol{\sigma} \right) \otimes \mathbf{Y}^k . \tag{47}$$

When the mechanical behavior is purely elastic (i.e., $\forall k = 1,...,2N_s : \dot{\tilde{\gamma}}^k = 0$), Eq. (47) simplifies to the following form:

$$\boldsymbol{\ell} = \boldsymbol{\ell}^1 + \boldsymbol{\ell}^2 + \mathbf{c}^e . \tag{48}$$

3. Numerical aspects

The developed self-consistent model is implemented into ABAQUS/Standard FE code using a user-defined material (UMAT) subroutine. The general flowchart summarizing the different stages of the finite element simulations using this self-consistent model and the workflow among them are shown in Fig. 3. At the structural scale, the macroscopic equations are solved over a typical time increment $I_\Delta = \left[t_n, t_{n+1} = t_n + \Delta t \right]$. To follow the updated Lagrangian formulation usually adopted in UMAT implementation, the configuration at t_n is used as initial "updated" configuration for the integration of the rate macroscopic equations over I_Δ. Accordingly, the macroscopic deformation gradient $\mathbf{F}(t_n)$ reduces to $\mathbf{I}_2$. The inputs consist of the following macroscopic quantities: the Cauchy stress rotated in the corotational frame $\underline{\Sigma}(t_n)$, and the deformation gradient $\mathbf{F}(t_{n+1})$. One of the main outputs that need to be computed is the updated Cauchy stress rotated in the corotational frame $\underline{\Sigma}(t_{n+1})$. The implicit FE computation also requires the determination of the macroscopic stiffness matrix **DDSDDE** (according to ABAQUS terminology). Tensor $\mathbf{F}(t_{n+1})$ is used to approximate the macroscopic velocity gradient $\mathbf{G}$. This velocity gradient is used as input at the polycrystal scale to determine the macroscopic tangent modulus $\mathcal{L}$, by solving the self-consistent equations, and to update the macroscopic stress and state variables. The constitutive equations at the single crystal scale should be solved and then the microscopic tangent moduli should be evaluated to completely determine the macroscopic tangent modulus $\mathcal{L}$. The inputs at the single crystal scale consist of the following microscopic quantities: the velocity gradient $\mathbf{g}$, which can be determined from the macroscopic one $\mathbf{G}$ by the localization relation, the Cauchy stress $\boldsymbol{\sigma}(t_n)$ and the state variables $f^{gr}(t_n)$, $\boldsymbol{\sigma}^{gr}(t_n)$, $\tilde{\gamma}^{gr\,(k)}(t_n)$, $\boldsymbol{\mu}^{gr\,(k)}(t_n)$, $\mathbf{s}^{gr\,(k)}(t_n)$, $\boldsymbol{\eta}^{gr\,(k)}(t_n)$, $d^{gr\,(k)}(t_n)$ (called STATEV by using the classical terminology of ABAQUS). The different numerical details related to these computations are given in Sections 3.1, 3.2 and 3.3.
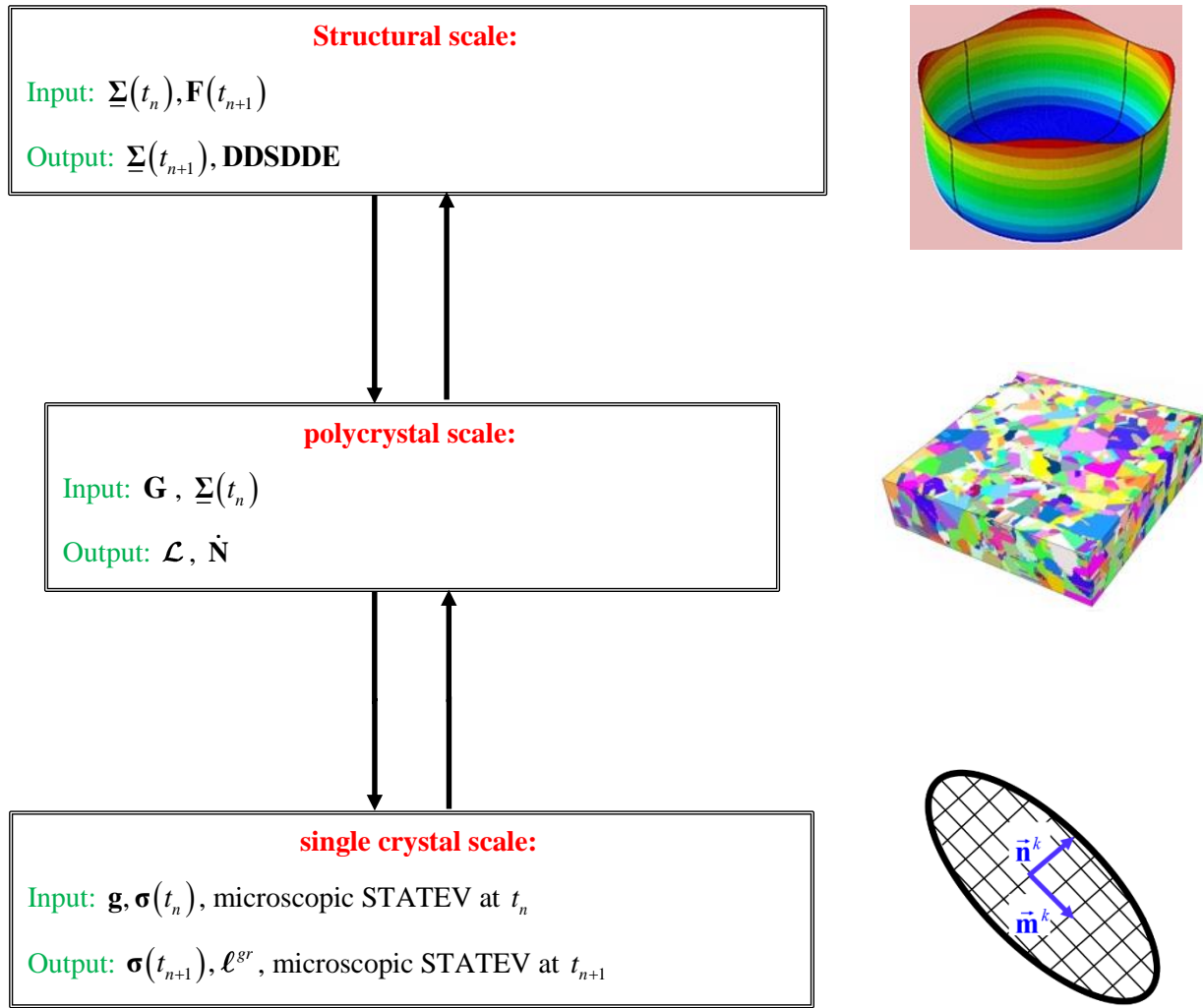
Fig. 3. Flowchart of the stages of the multiscale strategy embedding the self-consistent model in FEM.

3.1. Structural scale

To satisfy the objectivity principle (i.e., frame invariance), objective derivatives for tensor variables should be used. A practical approach, followed to guaranty frame invariance while maintaining simple forms of the constitutive equations, consists in reformulating these equations in a locally rotated current configuration (Eulerian by the eigenvalues of the variables and Lagrangian by its orientation). In the present work, a corotational approach based on the Jaumann objective rate is used. Accordingly, tensor quantities are expressed in a rotating frame so that simple material time derivatives can be used in the constitutive equations. This approach is consistent with the built-in formulation in ABAQUS/Standard FE code, where the constitutive equations are integrated in the corotational frame at the end of the time increment t_{n+1}. The inputs of the UMAT subroutine are the macroscopic Cauchy stress tensor at the beginning of the time increment, expressed in the corotational frame $\underline{\Sigma}(t_n)$, and the deformation gradient $\mathbf{F}(t_{n+1})$ evaluated with respect to the initial configuration. As to the outputs, these consist of

the structural unknowns: $\underline{\Sigma}(t_{n+1})$, and the macroscopic stiffness matrix **DDSDDE**. To determine these outputs, the self-consistent computations detailed in Section 3.2 need to be performed. The main input of these self-consistent computations is the macroscopic Eulerian velocity gradient **G** at the middle of the time increment, which is assumed to be constant over I_Δ and is given by the following approximate form [49]:

$$\mathbf{G} \approx \mathbf{G}(t_{n+1/2}) \approx \left(\frac{\mathbf{F}(t_{n+1}) - \mathbf{I}_2}{\Delta t}\right)\cdot\left(\frac{\mathbf{I}_2 + \mathbf{F}(t_{n+1})}{2}\right)^{-1}. \tag{49}$$

The structural unknowns $\underline{\Sigma}(t_{n+1})$ and **DDSDDE** will be determined on the basis of the subsequent developments. The rotated stress tensor $\underline{\Sigma}(t_{n+1})$ is determined from its counterpart $\Sigma(t_{n+1})$ by the following relation:

$$\underline{\Sigma}(t_{n+1}) = \Delta\mathbf{R}^T.\Sigma(t_{n+1}).\Delta\mathbf{R}, \tag{50}$$

where $\Delta\mathbf{R}$ is the increment of the rotation of the corotational frame over the time increment I_Δ. This rotation increment is obtained by the following relationship:

$$\Delta\mathbf{R} = \mathbf{e}^{\Delta t\,\mathbf{W}} \quad \text{with} \quad \mathbf{W} = \frac{1}{2}\left(\mathbf{G} - \mathbf{G}^T\right). \tag{51}$$

The macroscopic stress tensor $\Sigma(t_{n+1})$ required in Eq. (50) is calculated by the following explicit relationship:

$$\Sigma(t_{n+1}) = \Sigma(t_n) + \Delta t\,\dot{\Sigma}(t_n), \tag{52}$$

where tensor $\Sigma(t_n)$ is obtained from the input rotated tensor $\underline{\Sigma}(t_n)$ by:

$$\Sigma(t_n) = \Delta\mathbf{R}.\underline{\Sigma}(t_n).\Delta\mathbf{R}^T, \tag{53}$$

and $\dot{\Sigma}(t_n)$ is determined from the following relation:

$$\dot{\mathbf{N}}(t_n) = \dot{\Sigma}(t_n) + tr(\mathbf{G})\Sigma(t_n) - \mathbf{G}.\Sigma(t_n) \Leftrightarrow \dot{\Sigma}(t_n) = \dot{\mathbf{N}}(t_n) - tr(\mathbf{G})\Sigma(t_n) + \mathbf{G}.\Sigma(t_n), \tag{54}$$

which can be considered as the macroscopic counterpart of Eq. (38). The nominal stress rate $\dot{\mathbf{N}}(t_n)$ required in Eq. (54) to compute $\dot{\Sigma}(t_n)$ is given by the self-consistent computations of Section 3.2. Once $\dot{\Sigma}(t_n)$ is computed following Eq. (54), it is inserted in Eq. (52) to determine $\Sigma(t_{n+1})$. Then, the updated stress is rotated following Eq. (50) to compute $\underline{\Sigma}(t_{n+1})$. *In order to simplify the presentation of the following numerical developments of Sections 3.1, 3.2, and 3.3, reference to time t_n might be dropped, with the understanding that, if not indicated, the corresponding variable is evaluated at t_n.*

Now the expression of the macroscopic stiffness matrix **DDSDDE** should be determined from the expression of the macroscopic tangent modulus $\mathcal{L}$. To be consistent with the formulation followed in ABAQUS [50], this matrix is defined as the relationship between the Jaumann derivative of the macroscopic Kirchhoff stress tensor $\mathbf{K}^\nabla$ and the macroscopic strain rate $\mathbf{D}$ (the symmetric part of $\mathbf{G}$):

$$\mathbf{K}^\nabla = J\left(\mathbf{DDSDDE}\right):\mathbf{D}. \tag{55}$$

By using an updated macroscopic Lagrangian formulation (i.e. $J=1$), the Jaumann derivative $\mathbf{K}^\nabla$ is related to the time derivative $\dot{\boldsymbol{\Sigma}}$ as follows:

$$\mathbf{K}^\nabla = \dot{\boldsymbol{\Sigma}} + \boldsymbol{\Sigma}\, tr\left(\mathbf{G}\right) - \mathbf{W}.\boldsymbol{\Sigma} + \boldsymbol{\Sigma}.\mathbf{W}. \tag{56}$$

The combination of Eqs. (54) and (56) allows us to obtain the following relationship between $\mathbf{K}^\nabla$ and $\dot{\mathbf{N}}$:

$$\mathbf{K}^\nabla = \dot{\mathbf{N}} + \mathbf{G}.\boldsymbol{\Sigma} - \mathbf{W}.\boldsymbol{\Sigma} + \boldsymbol{\Sigma}.\mathbf{W}. \tag{57}$$

Introducing $\dot{\mathbf{N}} = \mathcal{L}:\mathbf{G}$ and $\mathbf{G} = \mathbf{D} + \mathbf{W}$ into Eq. (57), one obtains:

$$\mathbf{K}^\nabla = \mathcal{L}:\mathbf{G} + \mathbf{D}.\boldsymbol{\Sigma} + \boldsymbol{\Sigma}.\mathbf{W}. \tag{58}$$

Equation (58) involves dependency of $\mathbf{K}^\nabla$ on $\mathbf{W}$. However, an ABAQUS/Standard UMAT only handles symmetric tangent moduli. Assuming that the dependence on $\mathbf{W}$ remains small compared to the dependence on $\mathbf{D}$, one can use the following symmetrized tangent modulus:

$$DDSDDE_{ijkl} = \frac{1}{2}\left(\mathcal{L}_{ijkl} + \mathcal{L}_{ijlk}\right) + \delta_{ik}\Sigma_{jl}. \tag{59}$$

To completely solve the numerical problem formulated at the structural scale, both the macroscopic tangent modulus $\mathcal{L}$ and the macroscopic nominal stress rate $\dot{\mathbf{N}}$ need to be evaluated. This is the main task of the polycrystal scale computations presented in Section 3.2.

3.2. Polycrystal scale

The polycrystal algorithm aims to determine the macroscopic nominal stress rate $\dot{\mathbf{N}}$ and the tangent modulus $\mathcal{L}$ for a given macroscopic velocity gradient $\mathbf{G}$. Due to the mutual dependency between the localization tensor $\mathbf{A}^{gr}$, the microscopic tangent modulus ℓ^{gr}, and $\mathcal{L}$, the iterative fixed-point algorithm is used to solve the self-consistent constitutive equations. Alternatively, a Newton–Raphson scheme, as described in Appendix C, should be used. Selection of the fixed-point algorithm will be motivated in the results section.

The fixed-point algorithm is defined by the following main steps:

- *Step 0*: set the first guess for the macroscopic tangent modulus $\mathcal{L}^{(0)}$ and the tangent moduli $\ell^{gr\,(0)}$

to their converged values at the previous increment.

- *Step 1*: for $i \geq 1$, compute:

  - the interaction tensor $\mathbf{T}^{gr(i)}$ by using the numerical scheme developed by Berveiller et al. [46].

  - the localization tensor $\mathbf{A}^{gr(i)}$ by using the iterative form of Eq. (8):

  $$\mathbf{A}^{gr(i)} = \left(\mathbf{I}_4 - \mathbf{T}^{gr(i)} : \left(\ell^{gr(i-1)} - \mathcal{L}^{(i-1)} \right) \right)^{-1} : \left(\sum_{I=1}^{Ngr} f^I \left(\mathbf{I}_4 - \mathbf{T}^{I(i)} : \left(\ell^{I(i-1)} - \mathcal{L}^{(i-1)} \right) \right)^{-1} \right)^{-1}. \tag{60}$$

  - the microscopic velocity gradient $\mathbf{g}^{gr(i)}$ by using the iterative form of Eq. (3):

  $$\mathbf{g}^{gr(i)} = \mathbf{A}^{gr(i)} : \mathbf{G}. \tag{61}$$

  - the microscopic tangent moduli $\ell^{gr(i)}$ by integrating the single crystal constitutive equations with the ith iteration $\mathbf{g}^{gr(i)}$ of the microscopic velocity gradient. The numerical aspects related to this integration will be detailed in Section 3.3.

- *Step 2*: compute the new iteration of the macroscopic tangent modulus $\mathcal{L}^{(i)}$ as follows:

  $$\mathcal{L}^{(i)} = \sum_{gr=1}^{Ngr} f^{gr} \ell^{gr(i)} : \mathbf{A}^{gr(i)}. \tag{62}$$

- *Step 3*: if $\left(\left\| \mathcal{L}^{(i)} - \mathcal{L}^{(i-1)} \right\|_2 / \left\| \mathcal{L}^{(i)} \right\|_2 \right) < 10^{-6}$ (with $\left\| \mathcal{L} \right\|_2 = \left(\sum_{i=1}^{3} \sum_{j=1}^{3} \sum_{k=1}^{3} \sum_{l=1}^{3} \left(\mathcal{L}_{ijkl} \right)^2 \right)^{1/2}$), then the

  convergence of the self-consistent scheme is reached. Else, set $i = i+1$ and go to *Step 1*.

When convergence is reached, the grain volume fraction is explicitly updated using the following equation:

$$f^{gr}(t_{n+1}) = \frac{f^{gr}(t_n) e^{\Delta t \, tr(\mathbf{g}^{gr})}}{\sum_{I=1}^{Ngr} f^I(t_n) e^{\Delta t \, tr(\mathbf{g}^I)}}, \tag{63}$$

where $\mathbf{g}^I$ is the converged microscopic velocity gradient corresponding to grain I.

3.3. Single crystal scale

As stated in Sections 3.2.1 and 3.2.2, the single crystal constitutive equations need to be integrated over the time increment $I_\Delta = [t_n, t_{n+1}]$ in order to complete the self-consistent computations. *For the sake of brevity, exponent '(i)' referring to the current iteration of the self-consistent computations and index 'gr' designating the grain number will be omitted in the following numerical developments of Section 3.3. Furthermore, it needs to be recalled that, the time may not be stated when quantities are expressed*

at t_n. To integrate the single crystal constitutive equations, we assume that the mechanical quantities: $\boldsymbol{\sigma}$, $\tilde{\gamma}^k$, $\boldsymbol{\mu}^k$, $\boldsymbol{\eta}^k$, d^k and τ_c^k for $k = 1,...,2N_s$ are known at t_n. The velocity gradient $\mathbf{g}$ is assumed to be constant over I_Δ and it is given by the localization relationship (61) for the current iteration of the self-consistent computation (detailed in Section 3.2). The aim of the single crystal integration is to compute $\boldsymbol{\sigma}$, $\tilde{\gamma}^k$, $\boldsymbol{\mu}^k$, $\boldsymbol{\eta}^k$, d^k and τ_c^k for $k = 1,...,2N_s$ at $t_{n+1} = t_n + \Delta t$ as well as the microscopic tangent modulus $\boldsymbol{\ell}$. The algorithms followed to compute these unknown variables depend on the adopted microscopic plastic flow rule.

3.3.1. DCSC

The DCSC is defined by a non-smooth yield locus as shown in Fig. 2. This non-smooth feature implies that all the CSSs cannot be simultaneously activated (i.e., their slip rates are not all strictly positive) during plastic loading. Consequently, during plastic loading, the whole set of CSSs can be partitioned into two sets: the set of active CSSs, denoted $\mathcal{A}$, and the complementary set denoted $\mathcal{NA}$:

$$\forall\, k \in \mathcal{A}: \quad \dot{\tilde{\gamma}}^k > 0 \quad ; \quad \forall\, k \in \mathcal{NA}: \quad \dot{\tilde{\gamma}}^k = 0. \tag{64}$$

To integrate the constitutive equations based on the DCSC, the ultimate algorithm developed by Akpama et al. [27] is extended to take into account the damage effects on the single crystal modeling. Following the spirit of this algorithm family, the integration of the single crystal constitutive equations is carried out over successive sub-increments $I_\delta = [t_n, t_{n+\delta n} = t_n + \delta t] \subset I_\Delta$. The end of each sub-increment I_δ corresponds to a change in the set of active CSSs (through addition of new systems or suppression of existing systems). By analyzing the set of constitutive equations displayed in Section 2.2.3.1 and corresponding to the DCSC, one can easily deduce that the constitutive equations can be integrated once the slip rates of the active CSSs $\dot{\tilde{\gamma}}^k$ ($k \in \mathcal{A}$) as well as the length δt of I_δ are determined. Over each time sub-increment, this numerical problem can be viewed as a quadratic complementarity problem (QCP), which can be solved by the combinatorial search technique, for the identification of the set of active CSSs, and by the fixed-point method, for the computation of $\dot{\tilde{\gamma}}^k$ ($k \in \mathcal{A}$) and δt. The ultimate algorithm used to solve this QCP is defined by the following main steps:

- ▪ *Step 1*: determine the set of potentially active CSSs $\mathcal{P}$ defined as follows:

$$\mathcal{P} = \left\{ k = 1,...,2\,N_s: \quad \widehat{\tilde{\tau}}^k(t_n) - \tau_c^k(t_n) = 0 \right\}, \tag{65}$$

  where $\widehat{\tilde{\tau}}^k(t_n)$ is determined from the values of variables $\boldsymbol{\sigma}$, $\boldsymbol{\mu}^k$, $\boldsymbol{\eta}^k$ and d^k at t_n by combining Eqs. (18), (19), and (20). If $\mathcal{P} = \varnothing$ or { $\mathcal{P} \neq \varnothing$ and $\boldsymbol{\mu}^k : \tilde{\mathbf{c}}^e : \mathbf{d} \leq 0$ for all $k \in \mathcal{P}$ }, then the time sub-increment is purely elastic. In this case, the next step of this algorithm (*Step 2*) and the procedure developed in Section 3.3.1.1 to compute the slip rates are obviously avoided. Else, the sub-increment is elasto-plastic.

- *Step 2*: use the combinatorial method proposed by Anand and Kothari [18] to determine the set of active CSSs $\mathcal{A}$ from the set of potentially active CSSs $\mathcal{P}$. This method seems to be very efficient, as the search of active CSSs is reduced to the systems belonging to $\mathcal{P}$. The active CSSs remain active until the end of the sub-increment I_δ. Thus, the following equality holds for any system $k \in \mathcal{A}$:

$$\widehat{\overline{\tau}}^k\left(t_{n+\delta n}\right) - \tau_c^k\left(t_{n+\delta n}\right) = 0. \tag{66}$$

This equation can be reduced to the determination of the slip rates $\dot{\widehat{\gamma}}^k$ and the length δt of the sub-increment I_δ, over which criterion (17) remains valid. The numerical details related to this computation are given in Section 3.3.1.1.

- *Step 3*: update the different microscopic variables by using the update relations of Section 3.3.1.2.
- *Step 4*: if $\delta t < \Delta t$, then set $\Delta t = \Delta t - \delta t$ and $t_{n+\delta n} = t_n + \delta t$, and restart the computation from *Step 1* with a new time sub-increment. Else, this is the end of the ultimate incremental algorithm.

3.3.1.1. Computation of the slip rates of the active slip systems

By using Eqs. (16), (17) and (18), Eq. (66) can be rewritten as:

$$\forall k \in \mathcal{A}: \quad \tau^k\left(t_{n+\delta n}\right) + \alpha \sigma_\eta^k\left(t_{n+\delta n}\right)\sum_{l=1}^{2N_s} d^l\left(t_{n+\delta n}\right) = \sqrt{1 - d^k\left(t_{n+\delta n}\right)}\, \tau_c^k\left(t_{n+\delta n}\right). \tag{67}$$

The effective slip rates $\dot{\widehat{\gamma}}^k$ can be computed by solving the above set of non-linear equations. In these equations, product $\sqrt{1-d^k}\, \tau_c^k$ can be seen as an equivalent damaged critical shear stress and will be denoted in the following developments as $\tau_{c\ eq}^k$. To simplify the computation of the slip rates, $\tau_{c\ eq}^k$ is numerically assimilated to an internal variable. An Euler-forward scheme is used to expand the expressions of $d^k\left(t_{n+\delta n}\right)$ and $\tau_{c\ eq}^k\left(t_{n+\delta n}\right)$ in the following forms:

$$\forall k \in \mathcal{A}: \quad \begin{cases} d^k\left(t_{n+\delta n}\right) = d^k + \delta t\, \dot{d}^k = d^k + \delta t\, \dot{\widehat{\gamma}}^k\, \upsilon^k; \\ \tau_{c\ eq}^k\left(t_{n+\delta n}\right) = \tau_{ceq}^k + \delta t\, \dot{\tau}_{c\ eq}^k. \end{cases} \tag{68}$$

To avoid the difficulty induced by the consideration of the max function in the expression of $\sigma_\eta^k\left(t_{n+\delta n}\right)$, the subdivision of I_Δ into sub-increments is made such that there is no change in the sign of $\boldsymbol{\sigma} : \boldsymbol{\eta}^k$ during each sub-increment. Thus, (67) reads:

$$\forall k \in \mathcal{A}: \quad \boldsymbol{\mu}^k : (\boldsymbol{\sigma} + \delta\boldsymbol{\sigma}) + \alpha\, s^k \boldsymbol{\eta}^k : (\boldsymbol{\sigma} + \delta\boldsymbol{\sigma})\sum_{l=1}^{2N_s}\left(d^l + 2\delta t\, \dot{\widehat{\gamma}}^l \upsilon^l\right) = \tau_{c\ eq}^k + \delta t\, \dot{\tau}_{c\ eq}^k, \tag{69}$$

with $\delta\boldsymbol{\sigma} = \delta t\, \dot{\boldsymbol{\sigma}}^c$. Using the fact that each active slip k is potentially active at t_n, Eq. (69) can be reduced to the following rate form:

$$\forall k \in \mathcal{A}: \quad \left(\boldsymbol{\mu}^k + \alpha s^k \boldsymbol{\eta}^k \sum_{l=1}^{2N_s} \left(d^l + 2\delta t\, \dot{\tilde{\gamma}}^l v^l \right) \right) : \delta \boldsymbol{\sigma} + 2\alpha s^k \boldsymbol{\eta}^k : \boldsymbol{\sigma} \sum_{l=1}^{2N_s} \delta t\, \dot{\tilde{\gamma}}^l v^l = \delta t\, \dot{\tau}^k_{c\,eq}. \tag{70}$$

Indeed, for potentially active CSSs, we have the following equalities:

$$\forall k \in \mathcal{P}: \quad \boldsymbol{\mu}^k : \boldsymbol{\sigma} + \alpha s^k \boldsymbol{\eta}^k : \boldsymbol{\sigma} \sum_{l=1}^{2N_s} d^l = \tau^k_{c\,eq}. \tag{71}$$

The corotational stress rate $\dot{\boldsymbol{\sigma}}^c$, required to compute $\delta\boldsymbol{\sigma}$, can be derived from Eqs. (12), (22) and (42):

$$\dot{\boldsymbol{\sigma}}^c = \left(-\frac{1}{N_s} \dot{\tilde{\gamma}}^l v^l \mathbf{c}^e : \boldsymbol{\varepsilon}^e + \tilde{\mathbf{c}}^e : \left(\mathbf{d} - \frac{\dot{\tilde{\gamma}}^l\, \hat{\boldsymbol{\mu}}^l_{\mathbf{d}^p}}{\sqrt{1-d^l}} \right) \right) \quad ; \quad l = 1, \ldots, 2\,N_s. \tag{72}$$

Knowing that the effective slip rates $\dot{\tilde{\gamma}}^l$ are different from zero for only the active CSSs, Eq. (72) is reduced to the following form:

$$\dot{\boldsymbol{\sigma}}^c = \left(-\frac{1}{N_s} \dot{\tilde{\gamma}}^l v^l \mathbf{c}^e : \boldsymbol{\varepsilon}^e + \tilde{\mathbf{c}}^e : \left(\mathbf{d} - \frac{\dot{\tilde{\gamma}}^l\, \hat{\boldsymbol{\mu}}^l_{\mathbf{d}^p}}{\sqrt{1-d^l}} \right) \right) \quad ; \quad l \in \mathcal{A}. \tag{73}$$

In the meanwhile,

$$\forall k \in \mathcal{A}: \quad \dot{\tau}^k_{c\,eq} = -\frac{\dot{\tilde{\gamma}}^k v^k}{2\sqrt{1-d^k}} \tau^k_c + \sqrt{1-d^k}\, h^{kl} \dot{\tilde{\gamma}}^l \quad ; \quad l \in \mathcal{A}. \tag{74}$$

Thus, combining equations (70), (73), and (74), one can show that the slip rates of the active CSSs are solutions of the following quadratic system of equations:

$$\forall k \in \mathcal{A}: \quad A^{kl} \dot{\tilde{\gamma}}^l + H^{klm} \dot{\tilde{\gamma}}^l \dot{\tilde{\gamma}}^m = B^k \quad ; \quad l, m \in \mathcal{A}, \tag{75}$$

with

$$A^{kl} = -\left(\frac{1}{N_s} v^l \mathbf{c}^e : \boldsymbol{\varepsilon}^e + \frac{\tilde{\mathbf{c}}^e : \hat{\boldsymbol{\mu}}^l_{\mathbf{d}^p}}{\sqrt{1-d^l}} \right) : \hat{\boldsymbol{\mu}}^k_c + 2\alpha\, \sigma^k_\eta\, v^l + 2\delta t\, \alpha\, s^k v^l \boldsymbol{\eta}^\mathbf{k} : \tilde{\mathbf{c}}^e : \mathbf{d} + \frac{\delta^{kl} v^k}{2\sqrt{1-d^k}} \tau^k_c - \sqrt{1-d^k}\, h^{kl};$$

$$H^{klm} = -2\alpha\, s^k \boldsymbol{\eta}^k \delta t\, v^m : \left(\frac{1}{N_s} v^l \mathbf{c}^e : \boldsymbol{\varepsilon}^e + \frac{\tilde{\mathbf{c}}^e : \hat{\boldsymbol{\mu}}^l_{\mathbf{d}^p}}{\sqrt{1-d^l}} \right); \tag{76}$$

$$B^k = -\hat{\boldsymbol{\mu}}^k_c : \tilde{\mathbf{c}}^e : \mathbf{d}.$$

As shown in Eq. (76), matrices $\mathbf{A}$ and $\mathbf{H}$ depend on the length δt of the current sub-increment, which is not known a priori. Thus, there is a mutual dependency between the effective slip rates $\dot{\tilde{\gamma}}^k$ and δt. These unknowns should be determined simultaneously. To this aim, we have developed an iterative algorithm based on the following steps:

- *Step 0*: define the first guess for $\dot{\tilde{\gamma}}^k$ and δt as follows: $\forall k \in \mathcal{A}$: $\dot{\tilde{\gamma}}^{k(0)} = 0$ and $\delta t^{(0)} = \Delta t$.

- *Step 1*: for $i \geq 1$, compute $\mathbf{A}\!\left(\delta t^{(i-1)} \right)$ and $\mathbf{H}\!\left(\delta t^{(i-1)} \right)$ by using Eqs. (76).

- *Step 2*: estimate the effective slip rates $\dot{\hat{\gamma}}^{k(i)}$ as follows:

$$\forall k \in \mathcal{A}: \quad \dot{\hat{\gamma}}^{k(i)} = \widehat{A}^{kl}\left(\delta t^{(i-1)}\right).\left(B^l - H^{lmn}\left(\delta t^{(i-1)}\right)\dot{\hat{\gamma}}^{m(i-1)}\dot{\hat{\gamma}}^{n(i-1)}\right) \quad ; \quad l,m,n \in \mathcal{A}, \tag{77}$$

where $\widehat{\mathbf{A}}\left(\delta t^{(i-1)}\right)$ is the inverse of matrix $\mathbf{A}\left(\delta t^{(i-1)}\right)$.

- *Step 3*: on the basis of the effective slip rates $\dot{\hat{\gamma}}^{k(i)}$ computed in the previous step, determine the length $\delta t^{(i)}$ of the time sub-increment, over which inequality $(17)_1$ holds for all the inactive CSSs. This length can be obtained by the following minimization problem:

$$\delta t^{(i)} = \min_{k \in \mathcal{NA}}\left\{\Delta t, \widehat{\tilde{\tau}}^k\left(t_{n+\delta n}\right) \leq \tau_c^k\left(t_{n+\delta n}\right)\right\}. \tag{78}$$

- *Step 4*: the convergence of the computation of the effective slip rates and the length of the time sub-increment is reached, if the following conditions are fulfilled:

$$\left(\sum_{k \in \mathcal{A}}\left(A^{kl}\left(\delta t^{(i)}\right)\dot{\hat{\gamma}}^{l(i)} + H^{klm}\left(\delta t^{(i)}\right)\dot{\hat{\gamma}}^{l(i)}\dot{\hat{\gamma}}^{m(i)} - B^k\right)^2\right)^{1/2} \leq 10^{-12} \quad ; \quad l,m \in \mathcal{A}$$

$$\text{and} \quad \left|\delta t^{(i)} - \delta t^{(i-1)}\right| \leq 10^{-10}. \tag{79}$$

If these conditions are not fulfilled, the computations should be restarted from *Step 1* after taking $i = i+1$.

Through several numerical tests, we have observed that the above iterative algorithm rapidly converges (with less than 5 iterations). Thus, the introduction of the damage evolution does not lead to an important increase in the computation time required to integrate the single crystal constitutive equations. It is also important to recall that for the classical constitutive modeling (i.e., without consideration of the damage phenomenon), the quadratic form (75) is reduced to the following linear form:

$$\forall k \in \mathcal{A}: \quad A^{kl}\dot{\gamma}^l = B^k \quad ; \quad l \in \mathcal{A}, \tag{80}$$

with

$$\forall k,l \in \mathcal{A}: \quad A^{kl} = -\boldsymbol{\mu}^k : \mathbf{c}^e : \boldsymbol{\mu}^l - h^{kl} \quad ; \quad B^k = -\boldsymbol{\mu}^k : \mathbf{c}^e : \mathbf{d}. \tag{81}$$

In this case, the computation of the slip rates $\dot{\gamma}^k$ ($\forall k \in \mathcal{A}$) is performed in one iteration only, by simply multiplying vector $\mathbf{B}$ by the inverse of matrix $\mathbf{A}$.

Nevertheless, to ensure that the solution of the above iterative algorithm in terms of effective slip rates of active CSSs is unique, matrix $\mathbf{A}$ should be invertible at each iteration of this algorithm. Hence, the solution of the iterative scheme is not always unique. In the literature, there is no commonly agreed physical argument to choose one solution from the set of admissible solutions. Numerical methods have been proposed to overcome this issue [19], [26]. We have observed that this indetermination issue occurs only when the set of potentially active CSSs contains more than five CSSs, which means that the stress state $\boldsymbol{\sigma}$ at t_n is located in a degenerated vertex of the yield surface [26]. To avoid this situation, which

is due to the equality between the critical shear stresses, we have chosen to apply very slight random perturbations to the initial critical shear stresses. These perturbations allow us to decompose the degenerated vertices into simple ones and then to circumvent completely the indetermination problem during the computation. This method is physically relevant, as the equality between the critical shear stresses never actually happens, due to the heterogeneity of the defaults in the material.

3.3.1.2. Updating the different mechanical variables

Once the effective slip rates of the active CSSs and the length of the current time sub-increment are determined by the iterative algorithm of Section 3.3.1.1, the stress increment in the corotational frame should be computed by using Eq. (73). Then, the stress tensor in the initial configuration should be updated at $t_{n+\delta n} = t_n + \delta t$ as follows:

$$\boldsymbol{\sigma}\left(t_{n+\delta n}\right) = \mathbf{e}^{\delta t\, \mathbf{w}^e} \cdot \left(\boldsymbol{\sigma}\left(t_n\right) + \delta t \left(-\frac{1}{N_s} \dot{\tilde{\gamma}}^l \upsilon^l \mathbf{c}^e : \boldsymbol{\varepsilon}^e + \tilde{\mathbf{c}}^e : \left(\mathbf{d} - \frac{\dot{\tilde{\gamma}}^l \, \hat{\boldsymbol{\mu}}_{\mathbf{d}^p}^l}{\sqrt{1-d^l}} \right) \right) \right) \cdot \mathbf{e}^{-\delta t\, \mathbf{w}^e} \quad ; \quad l \in \mathcal{A} , \tag{82}$$

with

$$\mathbf{w}^e = \mathbf{w} - \mathbf{w}^p = \mathbf{w} - \frac{\dot{\tilde{\gamma}}^l}{\sqrt{1-d^l}} \mathbf{s}^l \quad ; \quad l \in \mathcal{A}. \tag{83}$$

Similarly, tensors $\boldsymbol{\mu}^k$, $\mathbf{s}^k$, $\boldsymbol{\eta}^k$ should be updated by the following relationships:

$$\forall k = 1,...,2\,N_s : \quad \begin{cases} \boldsymbol{\mu}^k\left(t_{n+\delta n}\right) = \mathbf{e}^{\delta t\, \mathbf{w}^e} \cdot \boldsymbol{\mu}^k\left(t_n\right) \cdot \mathbf{e}^{-\delta t\, \mathbf{w}^e} \; ; \\ \mathbf{s}^k\left(t_{n+\delta n}\right) = \mathbf{e}^{\delta t\, \mathbf{w}^e} \cdot \mathbf{s}^k\left(t_n\right) \cdot \mathbf{e}^{-\delta t\, \mathbf{w}^e} \; ; \\ \boldsymbol{\eta}^k\left(t_{n+\delta n}\right) = \mathbf{e}^{\delta t\, \mathbf{w}^e} \cdot \boldsymbol{\eta}^k\left(t_n\right) \cdot \mathbf{e}^{-\delta t\, \mathbf{w}^e} . \end{cases} \tag{84}$$

The damage variable d^k is updated following Eq. (68)[1]. Moreover, for the evolution of the critical shear stresses, the cumulated slip on each CSS should be computed by the following equation:

$$\forall k \in \mathcal{A}: \quad \tilde{\gamma}^k\left(t_{n+\delta n}\right) = \tilde{\gamma}^k\left(t_n\right) + \delta t\, \dot{\tilde{\gamma}}^k . \tag{85}$$

These updates should be stored and will be used for the integration of the single crystal constitutive equations for the next sub-increment.

To complement the resolution of the self-consistent equations in Section 3.2, the single crystal tangent modulus ℓ corresponding to the complete time increment I_A need to be evaluated. Due to the potential change in the activity of CSSs over I_A, this tangent modulus should be determined using the tangent moduli computed at the different time sub-increments by the following averaging formula:

$$\ell = \frac{1}{\Delta t} \sum_i \delta t_i \, \ell\left(t_i\right) . \tag{86}$$

Each intermediate tangent modulus $\ell(t_i)$ is determined by using Eq. (46) with the different microscopic quantities at the beginning of the current sub-increment t_i (namely $\boldsymbol{\sigma}$, v^k, $\boldsymbol{\mu}^k$, $\mathbf{s}^k$, $\boldsymbol{\eta}^k$, d^k) and vector $\mathbf{Y}^k(t_i)$, which is detailed in Appendix B.1.

3.3.2. DRSC

Contrary to the DCSC, there is no need to determine the set of active CSSs and to subdivide the time increment when the DRSC is used, since all the CSSs are simultaneously active during the plastic regime. By analyzing the constitutive equations defining the DRSC, one can observe that the main incremental unknowns over I_Δ are the plastic multiplier $\dot{\lambda}$ (one scalar unknown) and the components of $\dot{\boldsymbol{\sigma}}^c$ (six scalar unknowns). The equations to be solved to determine these unknowns are the incremental forms of Eq. (31) and Eq. (72). As for the DCSC, Eq. (31) has to be fulfilled at t_{n+1} considering explicit updates for the mechanical variables, which implies that the rate of mechanical variables used in Eq. (72) has to be considered at t_n. Particularly, the stress state used in Eq. (35) to compute κ^k (and consequently the slip rate) should be evaluated at t_n. However, to maintain the consistency of the flow rule, the stress state used to evaluate κ^k is expressed at t_{n+1}. Thus, the incremental forms of Eqs. (31) and (72) can be given as:

$$\tilde{f}_{reg}\left(t_{n+1}\right) = \sum_{k=1}^{N_s} \left(\frac{\tilde{\hat{\tau}}^k\left(t_{n+1}\right)}{\tau_c^k\left(t_{n+1}\right)}\right)^{2n} - 1 = \sum_{k=1}^{N_s}\left(\frac{\left(\boldsymbol{\sigma} + \Delta t\,\dot{\boldsymbol{\sigma}}^c\right):\left(\widehat{\boldsymbol{\mu}}_c^k + \Delta^c\widehat{\boldsymbol{\mu}}_c^k\right)}{\tau_{c\,eq}^k + \Delta t\,\dot{\tau}_{c\,eq}^k}\right)^{2n} - 1 = 0. \tag{87}$$

$$\boldsymbol{\sigma}^{err} := \dot{\boldsymbol{\sigma}}^c - \left[\tilde{\mathbf{c}}^e:\mathbf{d} - \dot{\lambda}\kappa^k\left(t_{n+1}\right)\left(\frac{v^k\mathbf{c}^e:\boldsymbol{\varepsilon}^e}{N_s} + \frac{\tilde{\mathbf{c}}^e:\widehat{\boldsymbol{\mu}}_{\mathbf{d}^p}^k}{\sqrt{1-d^k}}\right)\right] = \mathbf{0} \; ; \quad k = 1,...,2N_s, \tag{88}$$

where $\Delta^c\widehat{\boldsymbol{\mu}}_c^k$ is the increment of $\widehat{\boldsymbol{\mu}}_c^k$ in the lattice corotational frame. The new numerical system defined by Eqs. (87) and (88) is solved by the Newton–Raphson method. To construct the Jacobian matrix associated with the Newton–Raphson iterations, the following gradient functions should be evaluated: $\partial\tilde{f}_{reg}/\partial\dot{\boldsymbol{\sigma}}^c$, $\partial\tilde{f}_{reg}/\partial\dot{\lambda}$, $\partial\boldsymbol{\sigma}^{err}/\partial\dot{\boldsymbol{\sigma}}^c$ and $\partial\boldsymbol{\sigma}^{err}/\partial\dot{\lambda}$. These gradients are approximatively evaluated by neglecting the dependence of $\dot{\tau}_{c\,eq}^k$ and $\Delta^c\widehat{\boldsymbol{\mu}}_c^k$ on the main variables $\dot{\boldsymbol{\sigma}}^c$ and $\dot{\lambda}$. This reasonable choice allows significantly simplifying the computation of the gradients without slowing too much the convergence process. The analytical expressions of the components of the Jacobian matrix are given as follows:

$$\frac{\partial\tilde{f}_{reg}}{\partial\dot{\boldsymbol{\sigma}}^c}\left(t_{n+1}\right) = 2n\Delta t\sum_{k=1}^{N_s}\frac{\widehat{\boldsymbol{\mu}}_c^k + \Delta^c\widehat{\boldsymbol{\mu}}_c^k}{\tau_{c\,eq}^k\left(t_{n+1}\right)}\left(\frac{\tilde{\hat{\tau}}^k\left(t_{n+1}\right)}{\tau_c^k\left(t_{n+1}\right)}\right)^{2n-1} \quad ; \quad \frac{\partial\tilde{f}_{reg}}{\partial\dot{\lambda}}\left(t_{n+1}\right) = 0 \tag{89}$$

$$\frac{\partial \boldsymbol{\sigma}^{err}}{\partial \dot{\boldsymbol{\sigma}}^{c}} = \mathbf{I}_{4} + \dot{\lambda} \left(\frac{v^{k} \mathbf{c}^{e} : \boldsymbol{\varepsilon}^{e}}{N_{s}} + \frac{\tilde{\mathbf{c}}^{e} : \widehat{\boldsymbol{\mu}}_{\mathbf{d}^{p}}^{k}}{\sqrt{1-d^{k}}} \right) \otimes \frac{2n(2n-1)\,\Delta t}{\tau_{c}^{k}(t_{n+1})} \frac{\widehat{\boldsymbol{\mu}}_{c}^{k} + \Delta^{c} \widehat{\boldsymbol{\mu}}_{c}^{k}}{\tau_{c\,eq}^{k}(t_{n+1})} \left(\frac{\widetilde{\tau}^{k}(t_{n+1})}{\tau_{c}^{k}(t_{n+1})} \right)^{2n-2} \; ; \quad k=1,...,N_{s} \tag{90}$$

$$\frac{\partial \boldsymbol{\sigma}^{err}}{\partial \dot{\lambda}} = \kappa^{k}(t_{n+1}) \left(\frac{1}{N_{s}} v^{k} \mathbf{c}^{e} : \boldsymbol{\varepsilon}^{e} + \frac{\tilde{\mathbf{c}}^{e} : \widehat{\boldsymbol{\mu}}_{\mathbf{d}^{p}}^{k}}{\sqrt{1-d^{k}}} \right) \; ; \quad k=1,...,2N_{s}. \tag{91}$$

This iterative algorithm shows fast convergence when the regularization exponent n takes low values (typically lower than 50). However, when n is higher than 50, some convergence issues may occur (especially if the length Δt of the current time increment is relatively large, or if the loading path is complex). Indeed, in this case, a slight change in $\dot{\boldsymbol{\sigma}}^{c}$ could induce an important overtaking of the ratio $\left(\widetilde{\tau}^{k} / \tau_{c}^{k} \right)^{2n-1}$, which sometimes causes failure of convergence for the Newton–Raphson algorithm. To avoid this problem, during each Newton–Raphson iteration, the stress state is radially projected on the current yield surface before being used to update the internal variables and to compute the Jacobian matrix for the next iteration. In practice, for a stress state $\boldsymbol{\sigma}$ such that $\tilde{f}_{reg}(\boldsymbol{\sigma}) > 0$, the radial projection consists in finding a positive scalar θ defined such that:

$$\tilde{f}_{reg}(\theta \, \boldsymbol{\sigma}) = 0 . \tag{92}$$

The overall integration algorithm for the integration of the DRSC constitutive equations is defined by the following steps:

- *Step 0*: define the first guess for $\dot{\boldsymbol{\sigma}}^{c}$ and $\dot{\lambda}$ as follows: $\dot{\boldsymbol{\sigma}}^{c(0)} = \theta \, \tilde{\mathbf{c}}^{e} : \mathbf{d}$, with θ being such that $\tilde{f}_{reg}(\boldsymbol{\sigma} + \theta \, \tilde{\mathbf{c}}^{e} : \mathbf{d}) = 0$, and $\dot{\lambda}^{(0)} = \dot{\lambda}(t_{n})$.

- *Step 1*: for $i \geq 1$, use Eqs. (87)–(91) to compute the error function and the associated Jacobian matrix:

$$\begin{bmatrix} \tilde{f}_{reg}^{(i)} \\ \boldsymbol{\sigma}^{err(i)} \end{bmatrix} \quad \text{and} \quad \begin{bmatrix} \left(\dfrac{\partial \tilde{f}_{reg}}{\partial \dot{\boldsymbol{\sigma}}^{c}} \right)^{(i)} & \left(\dfrac{\partial \tilde{f}_{reg}}{\partial \dot{\lambda}} \right)^{(i)} \\ \left(\dfrac{\partial \boldsymbol{\sigma}^{err}}{\partial \dot{\boldsymbol{\sigma}}^{c}} \right)^{(i)} & \left(\dfrac{\partial \boldsymbol{\sigma}^{err}}{\partial \dot{\lambda}} \right)^{(i)} \end{bmatrix} . \tag{93}$$

- *Step 2*: compute the new iteration of the unknown vector:

$$\begin{bmatrix} \dot{\boldsymbol{\sigma}}^{c(i+1)} \\ \dot{\lambda}^{(i+1)} \end{bmatrix} = \begin{bmatrix} \dot{\boldsymbol{\sigma}}^{c(i)} \\ \dot{\lambda}^{(i)} \end{bmatrix} - \begin{bmatrix} \left(\dfrac{\partial \tilde{f}_{reg}}{\partial \dot{\boldsymbol{\sigma}}^{c}} \right)^{(i)} & \left(\dfrac{\partial \tilde{f}_{reg}}{\partial \dot{\lambda}} \right)^{(i)} \\ \left(\dfrac{\partial \boldsymbol{\sigma}^{err}}{\partial \dot{\boldsymbol{\sigma}}^{c}} \right)^{(i)} & \left(\dfrac{\partial \boldsymbol{\sigma}^{err}}{\partial \dot{\lambda}} \right)^{(i)} \end{bmatrix}^{-1} \cdot \begin{bmatrix} \tilde{f}_{reg}^{(i)} \\ \boldsymbol{\sigma}^{err(i)} \end{bmatrix} . \tag{94}$$

- *Step 3*: update the stress tensor in the lattice corotational frame by using the following relation:

$$\underline{\boldsymbol{\sigma}}^{(i+1)}\left(t_{n+1}\right)=\underline{\boldsymbol{\sigma}}\left(t_n\right)+\Delta t\,\dot{\underline{\boldsymbol{\sigma}}}^{c(i+1)}. \tag{95}$$

Determine the radial projection by computing scalar θ as follows:

$$\tilde{f}_{reg}\left(\theta\,\underline{\boldsymbol{\sigma}}^{(i+1)}\left(t_{n+1}\right)\right)=0\,, \tag{96}$$

and replace $\dot{\underline{\boldsymbol{\sigma}}}^{c(i+1)}$ by

$$\dot{\underline{\boldsymbol{\sigma}}}^{c(i+1)}=\frac{1}{\Delta t}\left(\theta\,\underline{\boldsymbol{\sigma}}^{(i+1)}\left(t_{n+1}\right)-\underline{\boldsymbol{\sigma}}\left(t_n\right)\right). \tag{97}$$

- *Step 4*: compute the new evaluation of the effective slip rates $\dot{\tilde{\gamma}}^k$, the rates of the damage variables $\dot{d}^k$, and the equivalent critical shear stresses τ_{ceq}^k ($\forall k=1,...,2N_s$) by using Eqs. (35), (27), and (71), respectively.

- *Step 5*: use the variables computed in *Step 4* to recalculate the error vector $\begin{bmatrix}\tilde{f}_{reg}^{(i+1)}\\ \boldsymbol{\sigma}^{err(i+1)}\end{bmatrix}$. If the norm

  of the error vector is lower than 10^{-6}, the convergence of the iterative procedure is reached. Else, the computations should be restarted from *Step 1* after taking $i=i+1$.

The use of the truncated stress, obtained by radial projection, instead of the whole stress allows us to ensure the permanent convergence of the above iterative algorithm. However, and despite the numerical effort spent to solve this challenging numerical problem, this convergence remains slow for high values of the regularization exponent n. This question will be further discussed in the results section.

The previous algorithm is complemented by the update of the unknown mechanical variables, by using the same formulas as those given in Section 3.3.1.2, and by the computation of the microscopic tangent modulus. For this computation, the expression of vector $\mathbf{Y}^k$, given in Appendix B, is introduced into expression (46) of the tangent modulus ℓ.

4. Simulation results

The algorithms and numerical techniques presented in Section 3 are assessed through several numerical predictions. In a preliminary stage, the influence of the damage evolution on the single crystal behavior is analyzed. Then, the performances of DCSC and DRSC algorithms are compared, at both single crystal and polycrystal levels, where numerical stability, CPU times and the numerically predicted results are investigated for both algorithms. Hence, the DCRSC numerical strategy is presented and its performances are checked in comparison with the DCSC and the DRSC schemes. Finally, structural computations are performed to highlight the capability of the implemented numerical schemes in predicting the behavior and ductile fracture of polycrystalline materials.

4.1. Material parameters

For the different simulations, single crystals with face-centered cubic (FCC) crystallographic structure are considered. Nevertheless, the proposed numerical methodology remains quite general to be applied to any other crystallographic structure. In FCC single crystals, plastic deformation results from crystallographic slip along four slip planes $\{111\}$ and three slip directions $\langle 1\bar{1}0 \rangle$, thus leading to twelve CSSs (i.e., $N_s = 12$). The numbering of vectors $\underline{\vec{m}}^k$ and $\underline{\vec{n}}^k$, measured in the intermediate configuration related to the crystallographic lattice, is enumerated in Table 1.

Table 1. The numbering of the CSSs of FCC single crystal.

k	1	2	3	4	5	6	7	8	9	10	11	12
$\sqrt{3}\,\underline{\vec{n}}^k$		$\begin{Bmatrix} 1 \\ 1 \\ 1 \end{Bmatrix}$			$\begin{Bmatrix} -1 \\ 1 \\ 1 \end{Bmatrix}$			$\begin{Bmatrix} 1 \\ -1 \\ 1 \end{Bmatrix}$			$\begin{Bmatrix} 1 \\ 1 \\ -1 \end{Bmatrix}$	
$\sqrt{2}\,\underline{\vec{m}}^k$	$\begin{Bmatrix} 1 \\ -1 \\ 0 \end{Bmatrix}$	$\begin{Bmatrix} 1 \\ 0 \\ -1 \end{Bmatrix}$	$\begin{Bmatrix} 0 \\ 1 \\ -1 \end{Bmatrix}$	$\begin{Bmatrix} 1 \\ 1 \\ 0 \end{Bmatrix}$	$\begin{Bmatrix} 1 \\ 0 \\ 1 \end{Bmatrix}$	$\begin{Bmatrix} 0 \\ 1 \\ -1 \end{Bmatrix}$	$\begin{Bmatrix} 1 \\ 1 \\ 0 \end{Bmatrix}$	$\begin{Bmatrix} 1 \\ 0 \\ -1 \end{Bmatrix}$	$\begin{Bmatrix} 0 \\ 1 \\ 1 \end{Bmatrix}$	$\begin{Bmatrix} 1 \\ -1 \\ 0 \end{Bmatrix}$	$\begin{Bmatrix} 1 \\ 0 \\ 1 \end{Bmatrix}$	$\begin{Bmatrix} 0 \\ 1 \\ 1 \end{Bmatrix}$

The initial critical shear stress is assumed to be identical for all the CSSs and equal to τ^0. The evolution of the critical shear stresses is described by an isotropic nonlinear hardening model, for which the components of the interaction-hardening matrix $\mathbf{h}$ are given as follows (similar to the hardening matrix used in [48]):

$$\forall i, j = 1,..., N_s : \quad h_{ij} = h_1 \, e^{-h_2 \Gamma}, \tag{98}$$

where h_1 and h_2 are hardening parameters, and Γ is the accumulated total strain on all CSSs, equal to $\sum_{k=1}^{2N_s} \tilde{\gamma}^k$. The material parameters used in the different simulations are reported in Table 2.

Table 2. Material parameters.

Elasticity		Hardening			Damage				
E (GPa)	ν	τ^0 (MPa)	h_1 (MPa/s)	h_2	S (MPa)	α	β	m	Y_0 (MPa)
200	0.3	320	900	20	30	0.005	1	4	0

4.2. Single crystal simulations

To highlight the combined effect of the strong coupling between the crystallographic damage and the material behavior as well as the influence of the initial crystallographic orientation on the mechanical behavior, the following loading path:

$$\mathbf{f} = \mathbf{I}_2 + t\,\mathbf{a}^{11} \quad \text{with} \quad \mathbf{a}^{11} = \begin{bmatrix} 1 & 0 & 0 \\ 0 & 0 & 0 \\ 0 & 0 & 0 \end{bmatrix}, \tag{99}$$

is applied to two differently oriented FCC single crystals (with $\mathbf{I}_2$ the second-rank identity tensor and t the time). The first single crystal is defined by the initial orientation $[100][010][001]$, which corresponds to zero Euler angles ($\varphi_1 = \phi = \varphi_2 = 0°$); while the second single crystal is defined by the initial orientation $[210][\bar{1}20][001]$, corresponding to Euler angles: $\varphi_1 = 26.57°$, $\phi = 0°$ and $\varphi_2 = 0°$ (see Fig. 4). For the sake of brevity, the first (resp. second) single crystal will be indicated in what follows by $[100]$ (resp. $[210]$).
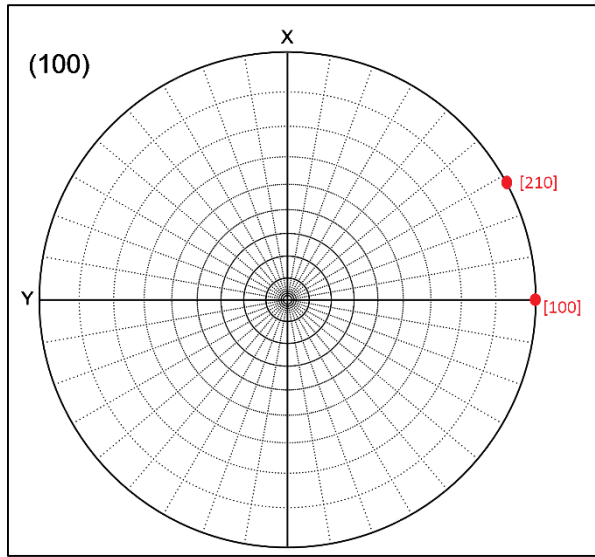
Fig. 4. Difference between the $[100]$ and $[210]$ initial orientations: (100) pole figure.

The time step Δt used to perform these single crystal simulations is set to 10^{-3} s. For comparison purposes, simulations for both damaged and undamaged single crystals are performed. In the numerical results presented in Fig. 5, Fig. 6 and Fig. 7, the classical Schmid criterion is used to describe the plastic flow rule (for both damaged and undamaged models). The evolution of the von Mises equivalent stress σ_{eq} is plotted in Fig. 5 as a function of the maximum eigenvalue of the logarithmic strain $\mathbf{le} = \ln\sqrt{\mathbf{f}.\mathbf{f}^T}$, denoted as le_{max}. For this particular loading path, le_{max} is identically equal to component $le_{11} = \ln(1 + \varepsilon_{11})$. At the beginning of the loading, the curves obtained by the DCSC coincide well with

those predicted by the CSC. Then, the discrepancy between the curves predicted by both models increases as the microscopic damage increases. As expected, the undamaged model exhibits a mechanical response that saturates with the plastic strain increase (considering Eq. (98) that defines the components of the hardening matrix). By contrast, strong softening is observed when the damage evolution is taken into account in the constitutive modeling. One may also notice that the effect of the initial crystalline orientation on the stress evolution is significant, as shown in the curves of Fig. 5. In fact, the difference in the initial orientation induces a difference in the activity of the CSSs and the corresponding accumulated slips, which leads to a difference in the hardening and damage evolutions and consequently in the evolution of the stress state.
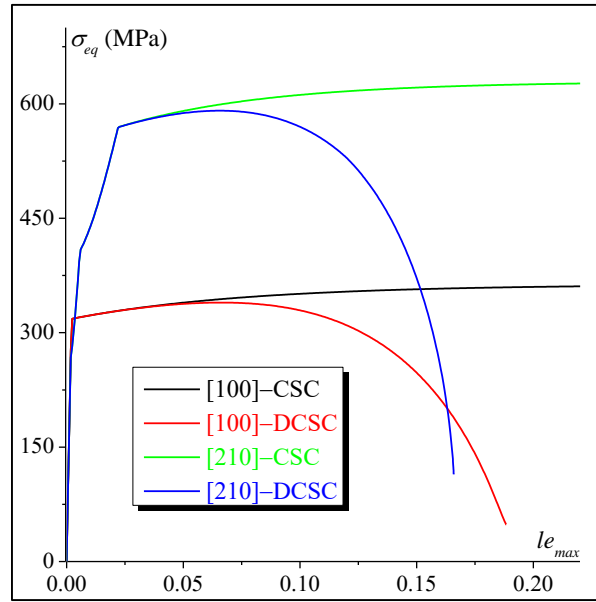
Fig. 5. Combined effect of damage and initial crystallographic orientation on the evolution of the equivalent stress σ_{eq} as a function of le_{max}.

The effect of the initial crystallographic orientation on the mechanical behavior can be better understood by analyzing the evolution of the accumulated slips for the active CSSs (Fig. 6). The results of Fig. 6 are obtained with the DCSC and remain quite similar to those obtained by the CSC (not presented here). For the $[100]$ orientation, five CSSs are active from the beginning to the end of the loading, with stable slip rates. As to the $[210]$ orientation, there is successive activation and deactivation of CSSs, leading to abrupt changes in the slip rates, which leads to non-smooth evolution of the stress state, as shown in Fig. 5. Moreover, for the $[210]$ orientation, plastic strain is mainly due to the activation of two dominant CSSs (namely systems 2 and 11). This concentration in the slip activity explains the faster failure in the grain defined by the $[210]$ initial orientation. Indeed, according to the damage evolution equation (see Eq. (27)), plastic strains concentrate on few CSSs, leading to a rapid increase of the damage variables inside the corresponding CSSs, and consequently, to a faster failure of the crystal. By contrast, for the

$[100]$ orientation, plastic strains are more homogeneously distributed over four CSSs (namely systems 2, 7, 8 and 16) from a total set of five active CSSs.
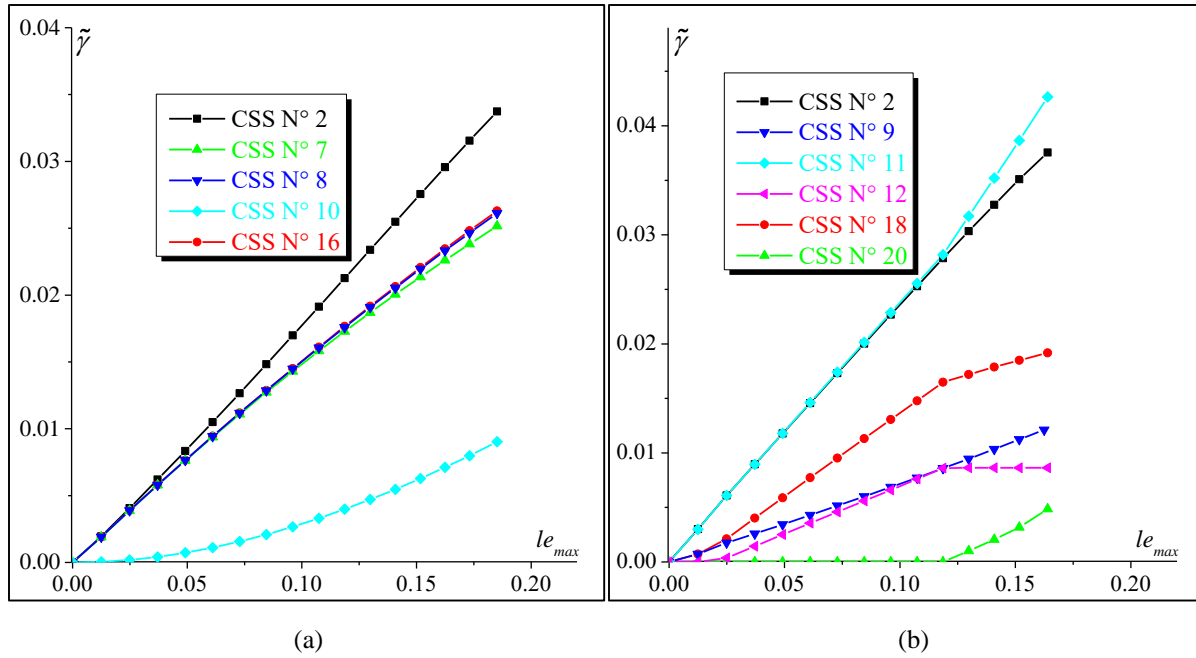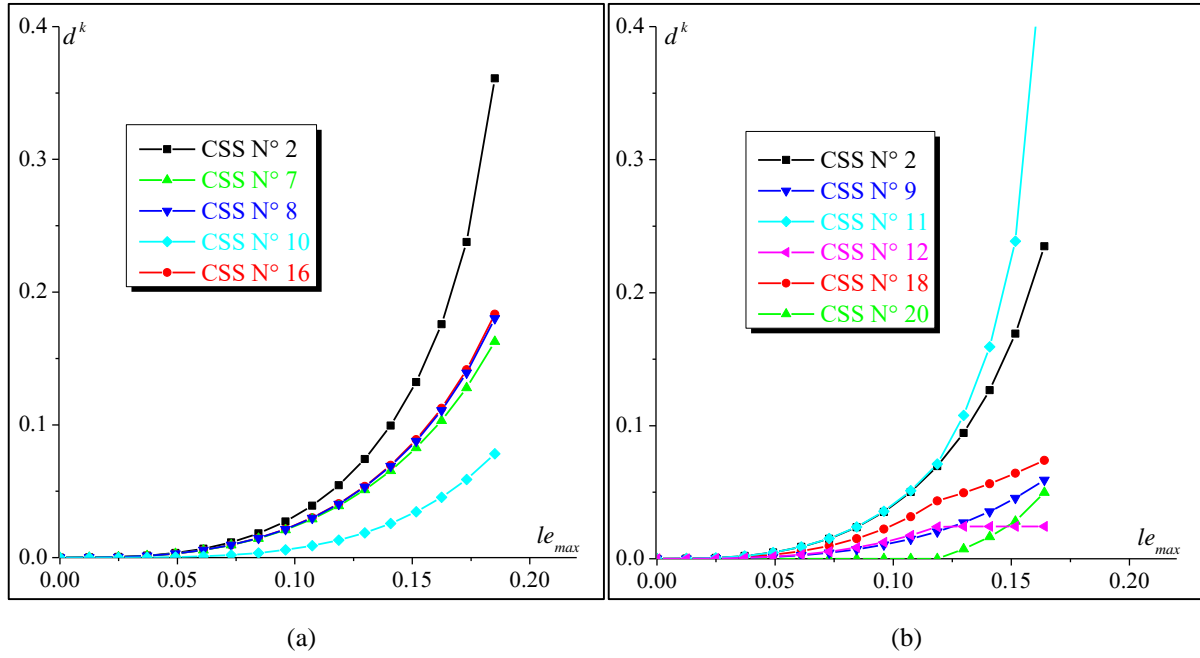

Fig. 6. Effect of the initial crystallographic orientation on the activity of the CSSs: (a) $[100]$ initial orientation; (b) $[210]$ initial orientation.

The results of Fig. 6 may be correlated to the evolution of the microscopic damage variables plotted in Fig. 7. As observed, damage increases more rapidly for the two main CSSs activated in the single crystal with $[210]$ initial orientation than for the four CSSs homogeneously activated in the $[100]$ single crystal.

Fig. 7. Effect of the initial crystallographic orientation on the damage evolution: (a) $[100]$ initial orientation; (b) $[210]$ initial orientation.

The predictions presented in Fig. 5, Fig. 6 and Fig. 7 are obtained using the CSC and DCSC algorithms and confirm the ability of these integration schemes to describe the coupling between the single crystal plasticity and the damage evolution. The DRSC algorithm is expected to provide results that are similar to those yielded by the DCSC, provided that high values are adopted for the regularization parameter n. To numerically investigate the effect of this regularization parameter on the single crystal predictions, we have applied two particular loading paths:

- The first loading (called LOAD1 in what follows) is defined such that only CSS N°1 is activated.

- The second loading (called LOAD2 in what follows) allows activating four CSSs (N°4, 6, 7 and 12).

To only activate CSS N°1, LOAD1 is defined by the following velocity gradient:

$$\mathbf{g} = \dot{\mathbf{f}}.\mathbf{f}^{-1} = \vec{\mathbf{m}}^1 \otimes \vec{\mathbf{n}}^1. \tag{100}$$

For this loading, the predictions obtained by the DRSC algorithm tend to those obtained by the DCSC when the regularization exponent n increases, as shown by the curves of Fig. 8. More specifically, the evolutions of all of the mechanical variables (equivalent stress, accumulated slips, and damage variables) predicted by the DCSC and the DRSC algorithms become perfectly similar for $n \geq 50$. Hence, the curves obtained by the DCSC and those given by the DRSC for $n \geq 50$ are almost indistinguishable. To analyze the effect of this regularization parameter on the evolution of the accumulated slip, attention is focused on two particular CSSs: CSS N°1, which is obviously activated considering the form (100) of the velocity gradient (Fig. 8b), and CSS N°16, which is inactive when

-33-

using the DCSC (Fig. 8c). The results of Fig. 8b and Fig. 8c confirm the trends observed for the equivalent stress: the accumulated slips (i.e., accumulated plastic strain) obtained by the DRSC algorithm tend to those obtained by the DCSC when exponent n takes large values. Also, the slip rates for CSS N°16 remain relatively high for low values of n, while they vanish as soon as n becomes larger than 50.
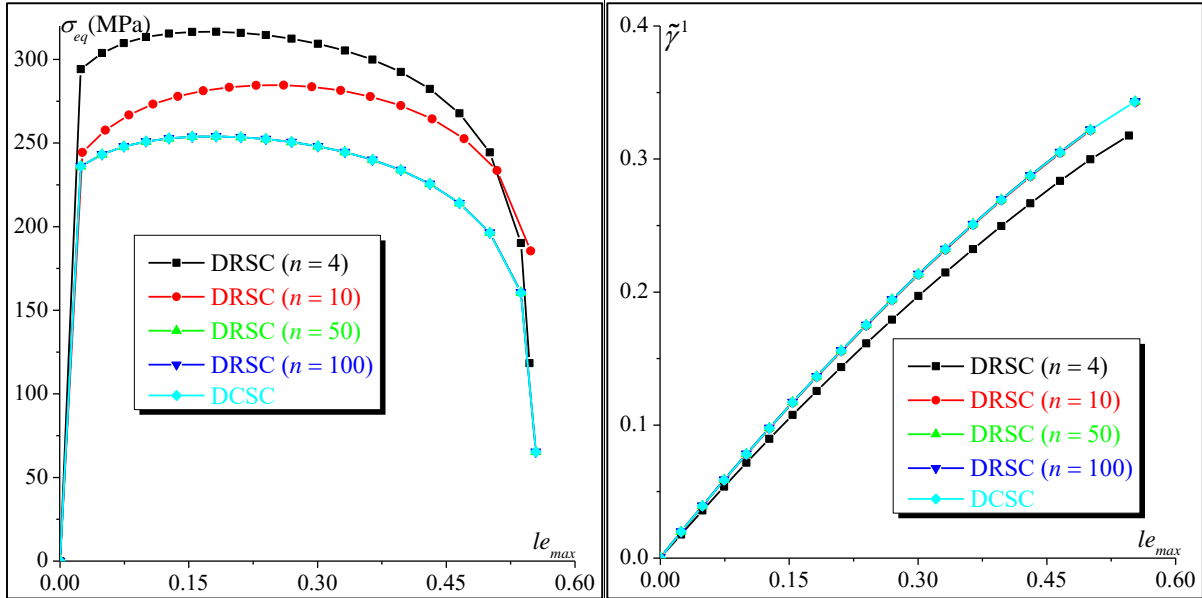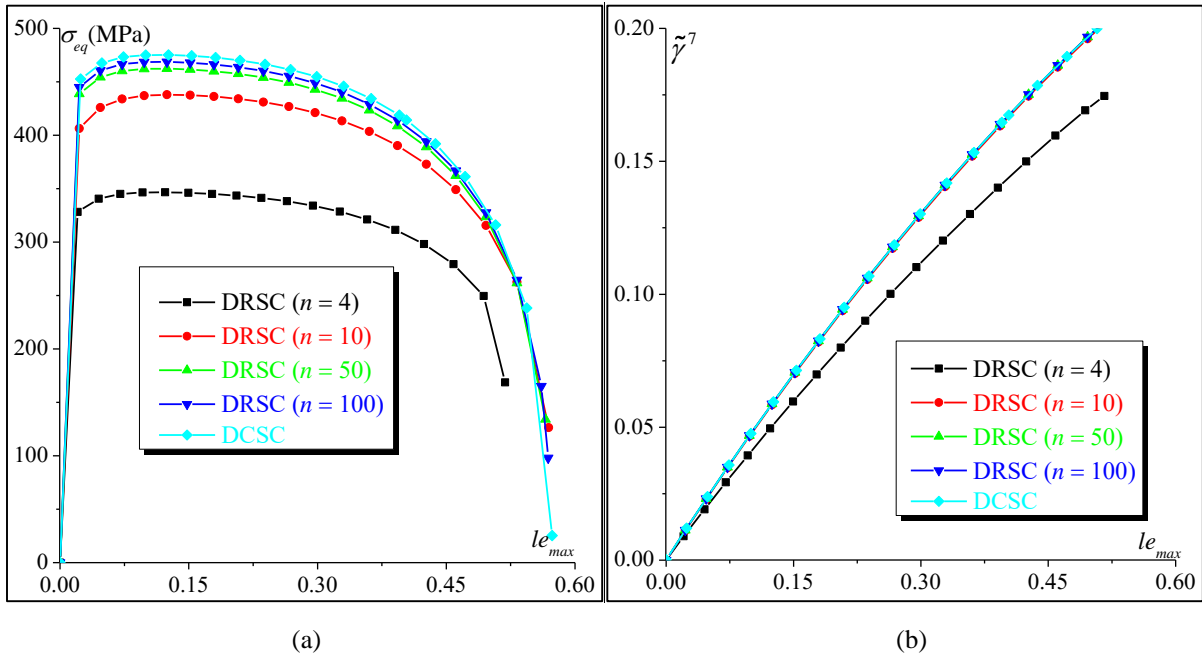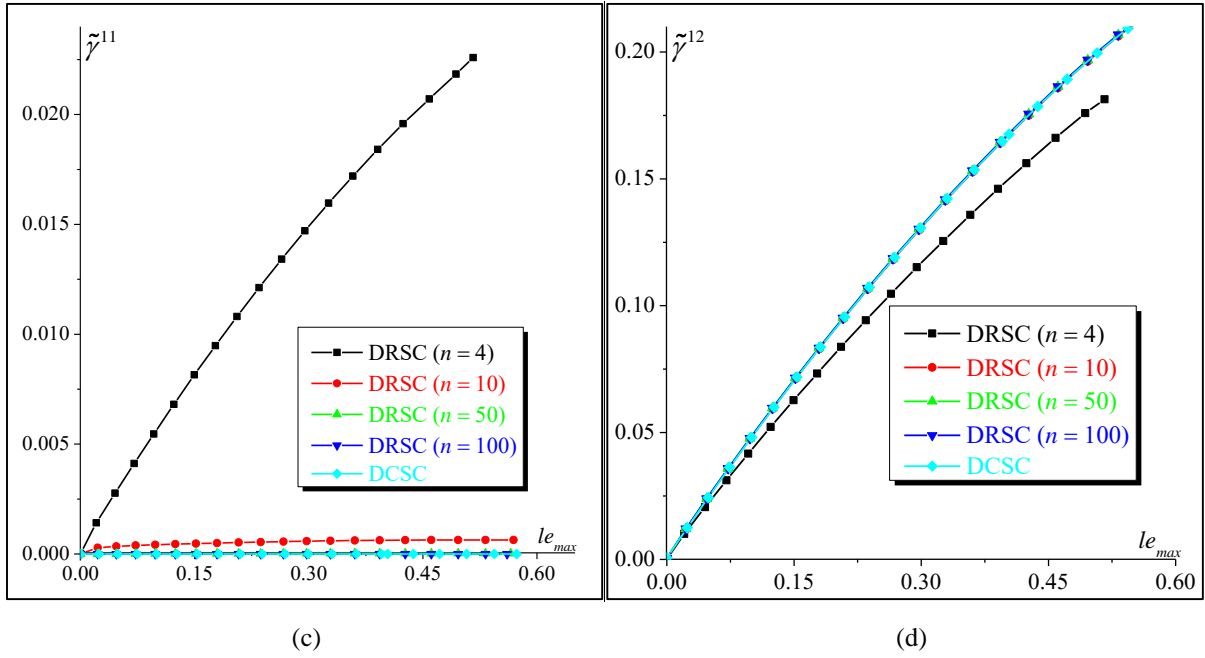

(a)

(b)
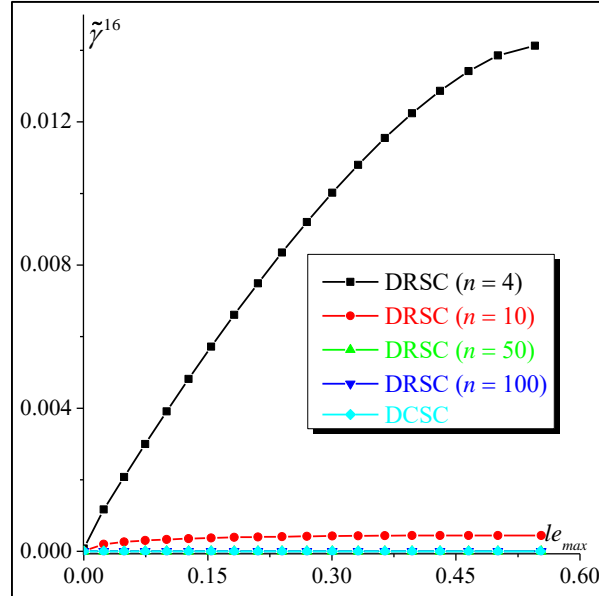
(c)

Fig. 8. Effect of the regularization exponent n on the predictions obtained for LOAD1: (a) the equivalent stress σ_{eq}; (b) the effective accumulated slip for CSS N°1 (active with the DCSC); (c) the effective accumulated slip for CSS N°16 (inactive with the DCSC).

To activate CSSs N°4, 6, 7 and 12, LOAD2 is defined by the following velocity gradient:

$$\mathbf{g} = \dot{\mathbf{f}}.\mathbf{f}^{-1} = \vec{\mathbf{m}}^4 \otimes \vec{\mathbf{n}}^4 + \vec{\mathbf{m}}^6 \otimes \vec{\mathbf{n}}^6 + \vec{\mathbf{m}}^7 \otimes \vec{\mathbf{n}}^7 + \vec{\mathbf{m}}^{12} \otimes \vec{\mathbf{n}}^{12}. \tag{101}$$

As shown in Fig. 9, the predictions obtained by both models (i.e., DCSC and DRSC) are quite similar for $n \geq 50$. A perfect match between the equivalent stress curves is observed for $n \geq 400$ (a result not presented in Fig. 9a). The need for high values of regularization exponent n for a perfect coincidence between the predictions given by the two models (as compared to LOAD1) is due to the slower convergence of the regularized yield surface associated with the DRSC algorithm when several CSSs are simultaneously active. For a better geometric interpretation of this phenomenon, the yield loci of Fig. 2 are examined. For LOAD1, the stress state predicted by the DCSC algorithm is obviously located on one plane of the yield locus, as only one CSS is active. In this case, a relatively low value of n is sufficient to obtain good agreement between stress states obtained by both models. For LOAD2, the stress state predicted by the DCSC scheme lies on a vertex of the yield function defined by the intersection of four slip planes, and consequently, a very high value of n is required to considerably reduce the difference between stress states predicted by both models.

(a)   (b)

(c)   (d)

Fig. 9. Effect of the regularization exponent n on the predictions obtained for LOAD2: (a) the equivalent stress σ_{eq} ; (b) the effective accumulated slip for CSS N°7 (active with DCSC); (c) the effective accumulated slip for CSS N°11 (inactive with DCSC); (d) the effective accumulated slip for CSS N°12 (active with DCSC).

The predictions presented in Fig. 8 and Fig. 9 demonstrate that the DCSC and DRSC algorithms give very similar results provided that the value of the regularization parameter n is sufficiently large (typically larger than 100). On the other hand, it is well known that the CPU time required for the integration of the constitutive equations based on the DRSC scheme substantially increases when the regularization parameter increases. To analyze the effect of this regularization parameter on the evolution of the computation time, a sensitivity study is performed. The results of this study are displayed in Fig. 10a, where the ratio of the CPU time required by the DRSC algorithm to that involved by the DCSC algorithm is plotted versus the regularization parameter n. This ratio, called 'CPU r$atio$' in Fig. 10a for shortness, ranges between 2.0 for $n=4$ and 14.0 for $n=250$, and is expected to monotonically increase with n. In fact, the number of iterations N_{iter}, required for the convergence of the Newton–Raphson scheme presented in Section 3.3.2 and used to solve the constitutive equations with the DRSC algorithm, increases with n, as shown in Fig. 10b. This is especially true at the beginning of the loading, when the stress evolution (and hence the shear stress evolution) is high enough. However, for relatively high accumulated plastic strain levels, the hardening tends to saturate and the evolution of the shear stresses becomes slower, and consequently, N_{iter} decreases in this stage. It must be pointed out that the loading applied here to plot the evolution of N_{iter} versus le_{max} is monotonic. As a consequence, the detrimental influence of a high regularization parameter on the CPU time is expected to be more critical for complex loading paths, in polycrystal FE computations.
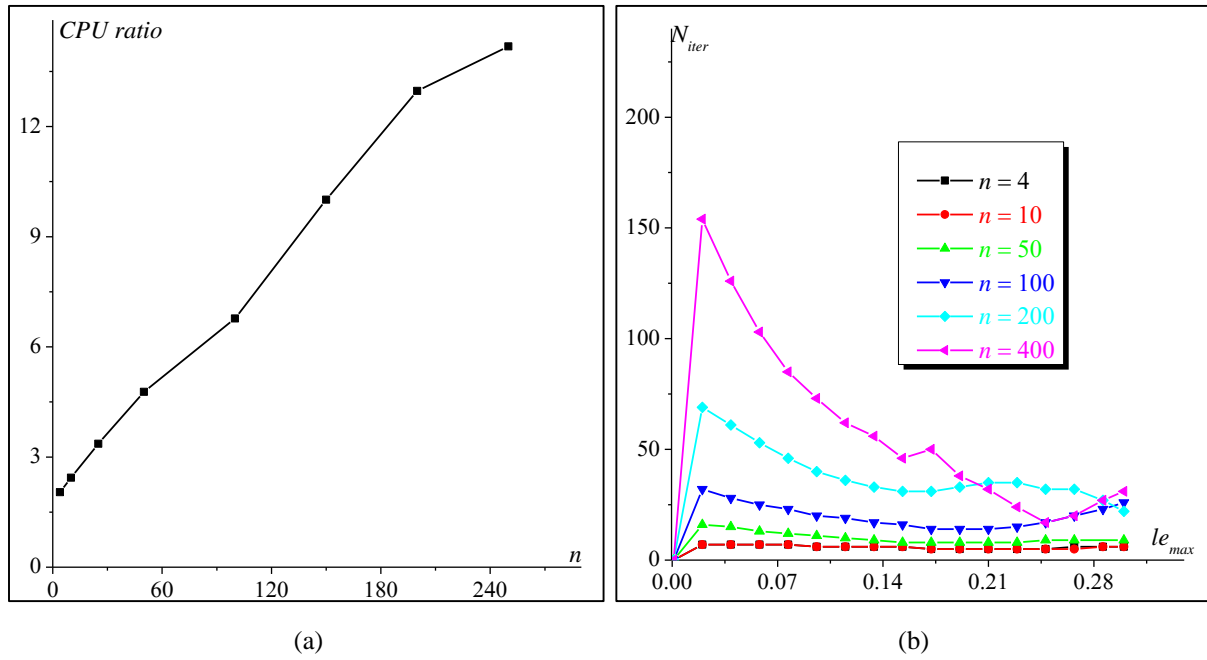
-36-

Fig. 10. Effect of the regularization parameter n on the computation effort: (a) CPU ratio; (b) Number of iterations of the Newton–Raphson scheme.

4.3. Polycrystal simulations

The numerical predictions at the single crystal level presented above reveal that the CPU time required by the DRSC algorithm is largely higher than that involved by the DCSC algorithm, especially for high values of n. This conclusion confirms the higher performance of the DCSC algorithm in producing efficient numerical predictions for the single crystal mechanical behavior. However, the set of active CSSs may change during plastic loading when the DCSC is used (see the details of the ultimate algorithm of Section 3.3.1). This potential evolution of the set of active CSSs leads to abrupt changes in the evolution of the microscopic tangent modulus components (Fig. 11), and causes severe convergence issues for the fixed-point method used to solve the self-consistent equations (see Eq. (46)). This drawback gets significantly worse for a polycrystalline aggregate, as this abrupt change is likely to be observed for a number of single crystals during the same time increment. Alternatively, the use of the DRSC algorithm allows obviously avoiding this problem, as all the CSSs are activated simultaneously. Indeed, the regularization of the Schmid criterion leads to a smooth evolution of the components of the microscopic tangent modulus, as shown in Fig. 11, thus considerably improving the convergence of the numerical algorithm used to solve the self-consistent equations. To combine the benefits of both algorithms (namely DCSC and DRSC) for the prediction of the polycrystalline behavior by the self-consistent approach, a mixed model named the DCRSC (damaged classical/regularized Schmid criterion) is proposed. The two following ingredients define this mixed model:

- At the single crystal scale, the evolutions of the stress tensor and the microscopic variables (plastic slip, damage…) are predicted by the DCSC algorithm. This choice guarantees the robust

and efficient integration of the single crystal constitutive equations.

- The microscopic tangent modulus, required to solve the self-consistent equations, is computed using Eq. (46) with matrix $\mathbf{Y}^k$ given by Eq. (B.16). All the microscopic variables required to compute this tangent modulus are predicted by the DCSC algorithm.
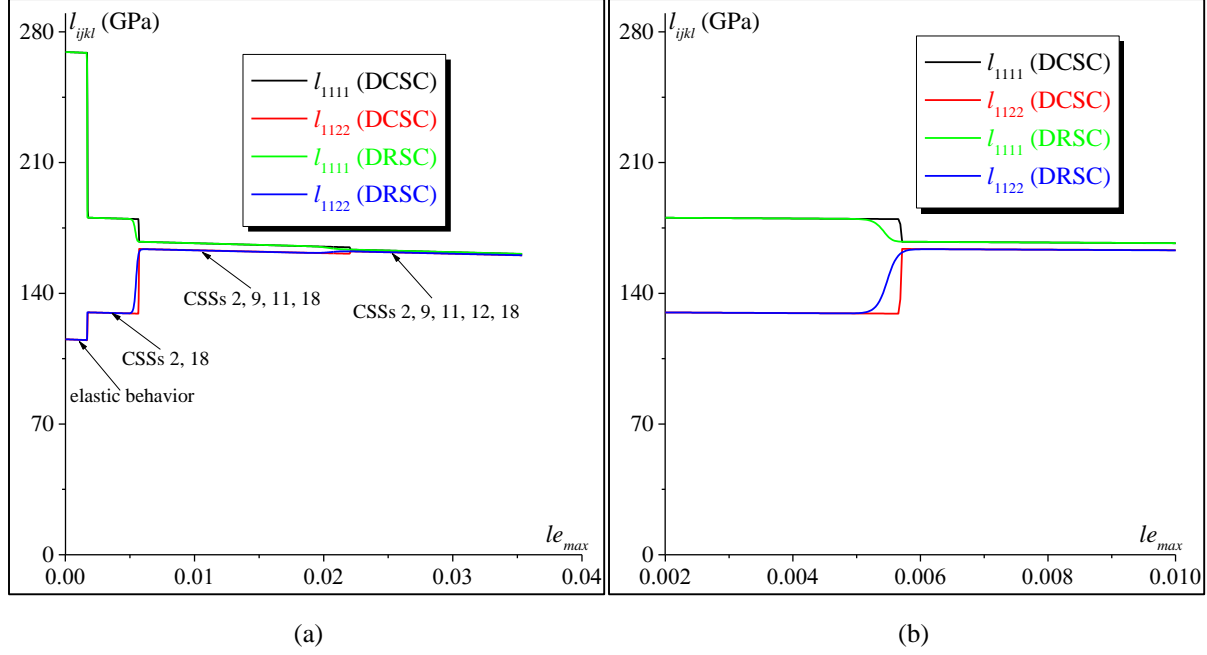

Fig. 11. Evolution of representative components of the microscopic tangent modulus ℓ : (a) $le_{max} \in [0,0.04]$; (b) zoom on the strain range $le_{max} \in [0.002, 0.01]$.

To compare the numerical predictions and performances of the three algorithms (DCSC, DRSC and mixed DCRSC), a polycrystalline aggregate with $Ngr = 1000$ grains is considered. The initial crystallographic orientations and volume fractions of the grains that compose this aggregate are randomly distributed. When the DRSC algorithm is used, the regularization parameter n is set to 100. Two different macroscopic loading paths are applied to the selected polycrystalline aggregate. The first loading (called hereafter LOAD3) does not involve any macroscopic rotation, and is defined by the following macroscopic deformation gradient:

$$\mathbf{F}^3 = \mathbf{I}_2 + E_{11}\,\mathbf{A}^{11} \quad \text{with} \quad \mathbf{A}^{11} = \begin{bmatrix} 1 & 0 & 0 \\ 0 & 0 & 0 \\ 0 & 0 & 0 \end{bmatrix}, \tag{102}$$

while the second macroscopic loading (designated as LOAD4) is defined by the following macroscopic deformation gradient:

$$\mathbf{F}^4 = \mathbf{I}_2 + \Gamma_{12}\,\mathbf{A}^{12} \quad \text{with} \quad \mathbf{A}^{12} = \begin{bmatrix} 0 & 2 & 0 \\ 0 & 0 & 0 \\ 0 & 0 & 0 \end{bmatrix}. \tag{103}$$

The application of LOAD4 leads to a non-zero macroscopic rotation, which is expected to induce more important crystallographic texture evolution than LOAD3. The use of the self-consistent scheme with an initially random crystallographic texture implies that the microscopic strain tensor is heterogeneous during the loading, and the microscopic loading paths are not necessarily linear, unlike the previous simulations with loading paths (LOAD1 and LOAD2).

To evaluate the macroscopic damage evolution, let us introduce the macroscopic damage measure, denoted as D^{poly}, and defined as the volume average of the microscopic damage variables d_{av}^{gr} [17]:

$$D^{poly} = \sum_{gr=1}^{Ngr} f^{gr}\, d_{av}^{gr} = \frac{1}{2N_s} \sum_{gr=1}^{Ngr} \sum_{k=1}^{2N_s} f^{gr} d^{gr\,(k)}. \tag{104}$$

This macroscopic damage measure should be viewed as a numerical damage indicator rather than a physical macroscopic damage variable. It has been used only to output the finite element results. Considering Eq. (104) defining D^{poly} as the double average over all the CSSs (inactive and active) and over all the constituent grains (independently of the severity of the loading applied on each grain), we expect that D^{poly} remains much smaller than 1 when the macroscopic failure is reached. The numerical predictions presented in Fig. 12b and Fig. 14b reveal indeed that D^{poly} remains lower than 0.1 at failure, and is mainly dependent on the applied loading. Note also that the microscopic elastic properties of the material are strongly affected by the microscopic damage variable d_{av}^{gr}, according to Eq. (13). This shows that, in the present constitutive modeling, damage strongly affects both the elastic behavior (Eq. (13)) and the plastic behavior (Eq. (25)).

LOAD3 is applied with the different algorithms as long as convergence is satisfied at both the single crystal and polycrystal scales. As shown in Fig. 12, the three algorithms (DCSC, DRSC and DCRSC) converge until a certain extent of damage-induced softening. However, when damage increases significantly enough, the DCSC and the DRSC algorithms encounter some convergence issues, which cause the computations to be prematurely stopped (as indicated by cross symbols in Fig. 12). Indeed, for the DCSC algorithm, the fixed-point method used to solve the self-consistent equations fails to converge, due to the abrupt change in the activity of CSSs for some grains. As to the DRSC algorithm, the convergence problem comes from the integration of the single crystal constitutive equations (as the regularization parameter is relatively high and the majority of single crystals are submitted to microscopic complex loading paths). However, the mixed algorithm (DCRSC) enables convergence up to the final stage of deformation. Also, as shown in Fig. 12a and b, the macroscopic results given by the three algorithms are quite similar. A slight difference is observed at the early stage of plastic flow, between the predictions given by DCSC on the one hand and those yielded by the DRSC and DCRSC

algorithms (Fig. 12a). This is due to the difference in the computation of the microscopic tangent modulus. The effect of the selected model on the microscopic behavior is analyzed in Fig. 12c, where the evolution of the microscopic equivalent stress for three grains is plotted as a function of LE_{max}. The numerical predictions of Fig. 12c confirm the results observed at the macroscopic level revealing the very good agreement between the predictions obtained by the DRSC and DCRSC algorithms. To further compare the performances of the different algorithms, the CPU time required to reach a macroscopic accumulated plastic strain level $LE_{max} = 0.12$ is recorded for the different simulations (the size of the time increment is taken the same for these simulations). It turns out from this comparative study that the DCSC and DCRSC algorithms require almost the same CPU time to reach the targeted strain level (with a slightly better performance for the DCRSC scheme in the softening stage). By contrast, the CPU time required by the DRSC algorithm is three times larger than the one needed for the DCRSC algorithm.

(a)　　　　　　　　　　　　　　　　(b)
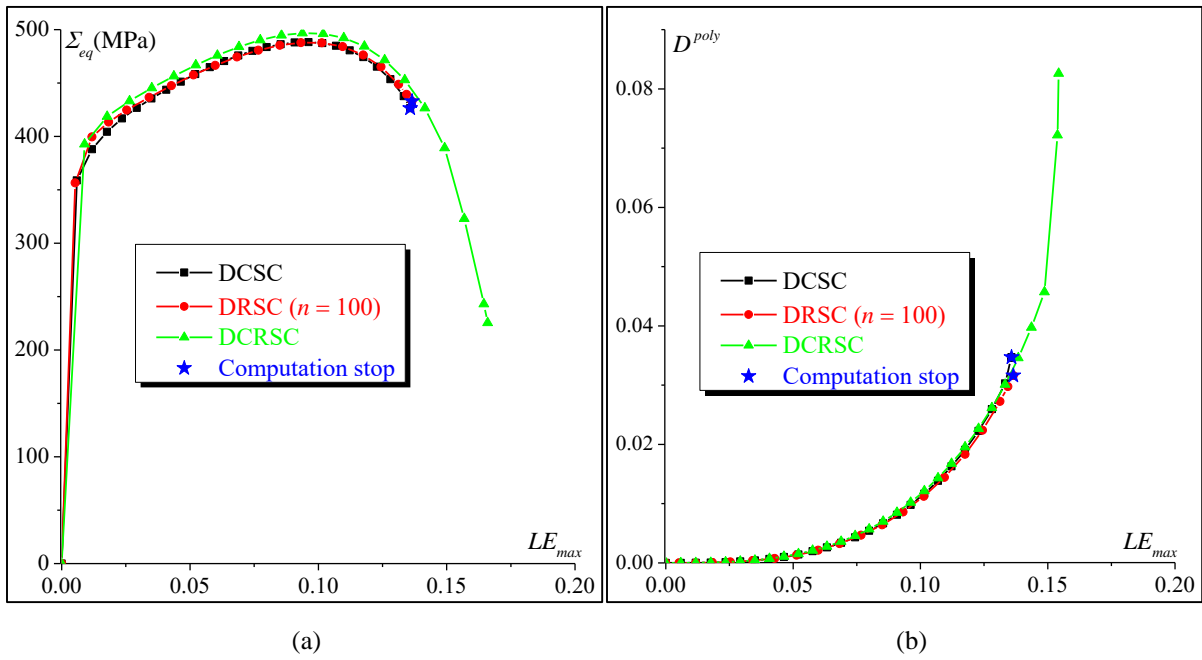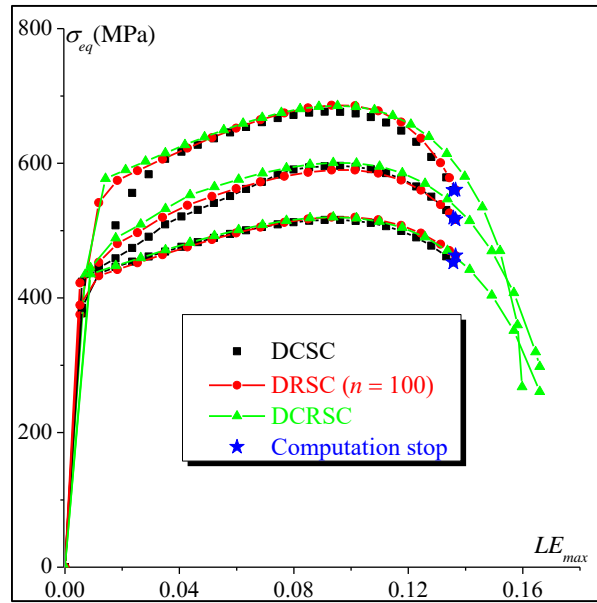
(c)

Fig. 12. Comparisons between the predictions obtained by the three numerical algorithms for LOAD3: (a) evolution of the macroscopic equivalent stress Σ_{eq}; (b) evolution of the macroscopic damage variable D^{poly}; (c) evolution of the microscopic equivalent stress σ_{eq} for three different grains.

The initial and final crystallographic textures predicted by both the DCSC and DCRSC algorithms are plotted in the form of (100) pole figures in Fig. 13. The final textures are predicted at the strain level that corresponds to convergence failure for the DCSC algorithm (see Fig. 12). The results of Fig. 13 confirm that the texture evolution is very slow and quite similar for the different algorithms. This result is expectable considering the fact that the crystallographic texture evolution is uniquely due to the single crystal rotation, while LOAD3 does not generate a macroscopic rotation.

| (a) | (b) | (c) |
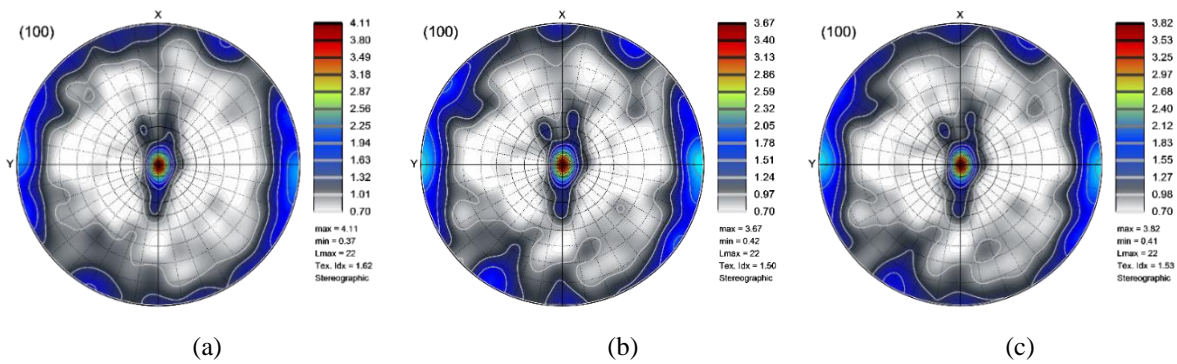
Fig. 13. Prediction of crystallographic texture: (a) Initial texture; (b) final texture obtained by the DCSC; (c) final texture obtained by the DCRSC. Poles figures generated using the ATEX software [51].

Similar to the observations relating to LOAD3, both the DCSC and DRSC algorithms encounter some convergence issues when LOAD4 is applied. As shown in Fig. 14a, the DCSC algorithm is unable to

achieve accumulated plastic strain levels higher than $LE_{max} \approx 0.05$, as the fixed-point method fails to converge at this value. By comparing the predictions of Fig. 12 and Fig. 14, one may notice that this convergence issue is more important for LOAD4 than for LOAD3. This early convergence failure of the self-consistent computations is mainly due to the frequent abrupt changes in the microscopic tangent modulus for several single crystals, caused by the persistent evolution of the activity of the CSSs during plastic loading. These frequent changes in the CSS activity can be explained by the fast evolution of the crystallographic rotation resulting from the presence of macroscopic rotation for LOAD4. The use of the iterative Newton–Raphson scheme shows the same convergence issue, as these abrupt changes in the CSS activity are not taken into consideration in the material Jacobian matrix computation (see Appendix C.2). This issue does not affect the convergence of the DRSC scheme. Indeed, the abrupt changes in the tangent modulus components are smoothed by the numerical regularization, as displayed in Fig. 11. Hence, for the DRSC numerical scheme, convergence is achieved until a high macroscopic strain level is reached (i.e., $LE_{max} \approx 0.2$), as shown in Fig. 14a. However, it fails before the end of the simulation (final fracture of the aggregate). In the same way as for LOAD3, this issue comes from the numerical difficulties encountered in the integration of the single crystal constitutive equations. In fact, at this loading stage, there are already several highly damaged grains, even if the polycrystal is globally undamaged (Fig. 14b). Indeed, LOAD4 induces strong localization of the microscopic plastic strain field within a few grains, causing them to be significantly damaged long before the other grains. On the other hand, the DCRSC algorithm leads the simulation up to failure of the polycrystal. Indeed, thanks to its construction (see Section 4.2.2.3), the DCRSC algorithm is not affected by the numerical difficulties preventing the DCSC and DRSC algorithms to converge. This confirms the robustness of this algorithm compared to the two others.
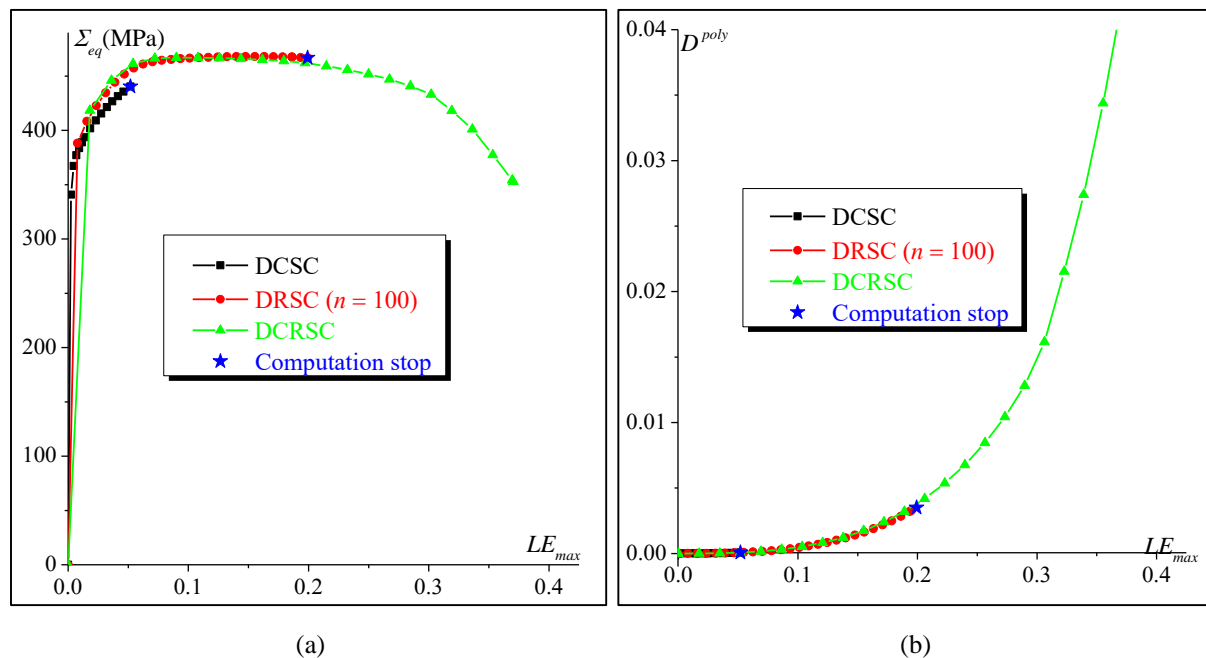
(a)   (b)

Fig. 14. Comparisons between the predictions obtained by the three numerical algorithms for LOAD4: (a) evolution of the macroscopic equivalent stress Σ_{eq} ; (b) evolution of the macroscopic damage variable D^{poly} .

The evolution of the crystallographic texture is presented in Fig. 15 in the form of (100) pole figures for different loading levels. To plot these figures, LOAD4 is applied using the DCRSC algorithm. As expected, this evolution is more significant than that predicted with LOAD3 (Fig. 13).

(a)   (b)   (c)

(d)   (e)
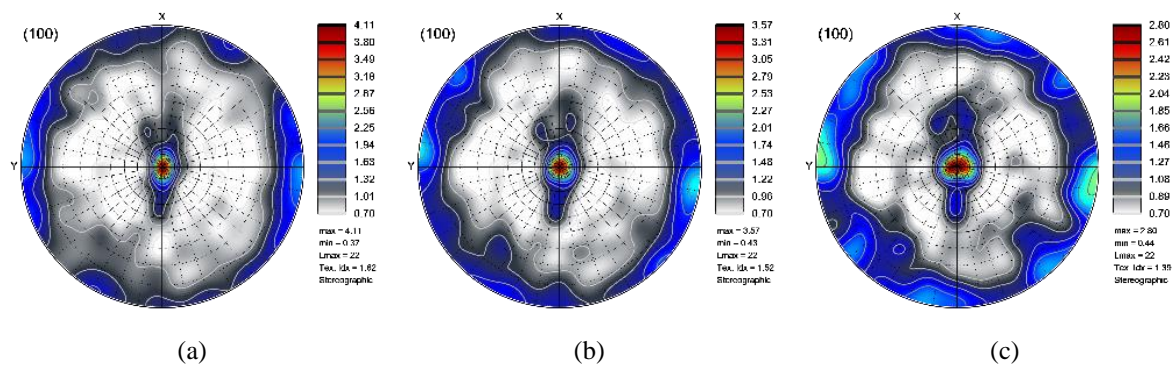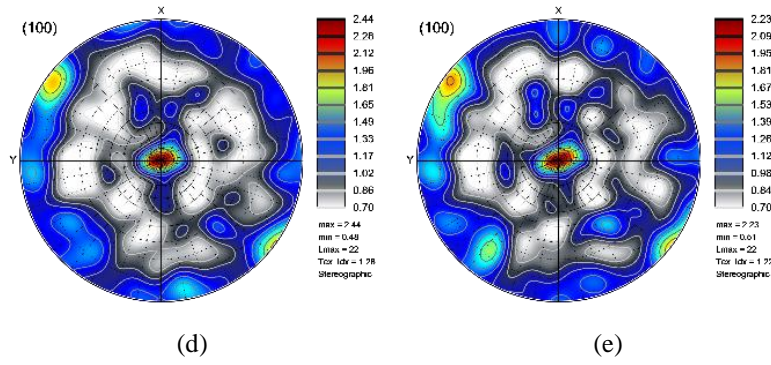
Fig. 15. Evolution of crystallographic texture: (a) $LE_{max} = 0$; (b) $LE_{max} = 0.10$; (c) $LE_{max} = 0.20$; (d) $LE_{max} = 0.30$; (e) $LE_{max} = 0.36$.

The efficiency of the fixed-point method in solving the self-consistent equations is evaluated by comparing the number of iterations and the CPU time that it requires to those required by the Newton–Raphson method. The main details of the resolution scheme of the self-consistent equations using the Newton–Raphson algorithm are provided in Appendix C. As shown in Fig. 16a, the number of iterations is lower for the Newton–Raphson scheme than for the fixed-point method. Nevertheless, the corresponding CPU time appears, in average, to be lower for the fixed-point method. For both iterative methods, the statistical distribution of the CPU time needed for calling the UMAT subroutine is studied and the corresponding relative density functions are shown in Fig. 16b. These distributions exhibit peaks of density for some CPU times. Comparing Fig. 16a to Fig. 16b, one can deduce, as indicated in Fig. 16b, the correspondence between peaks and numbers of iterations. Then it appears that, for a given number of iterations, the Newton–Raphson iterative scheme is much slower than the fixed-point algorithm. Indeed, this is due to the computation of the gradient operator and its inversion, which are highly time consuming. Therefore, the fixed-point method is globally faster than the Newton–Raphson scheme. It is worth noting that the simulations performed to establish the comparative study of Fig. 16 are based on the DCRSC algorithm.
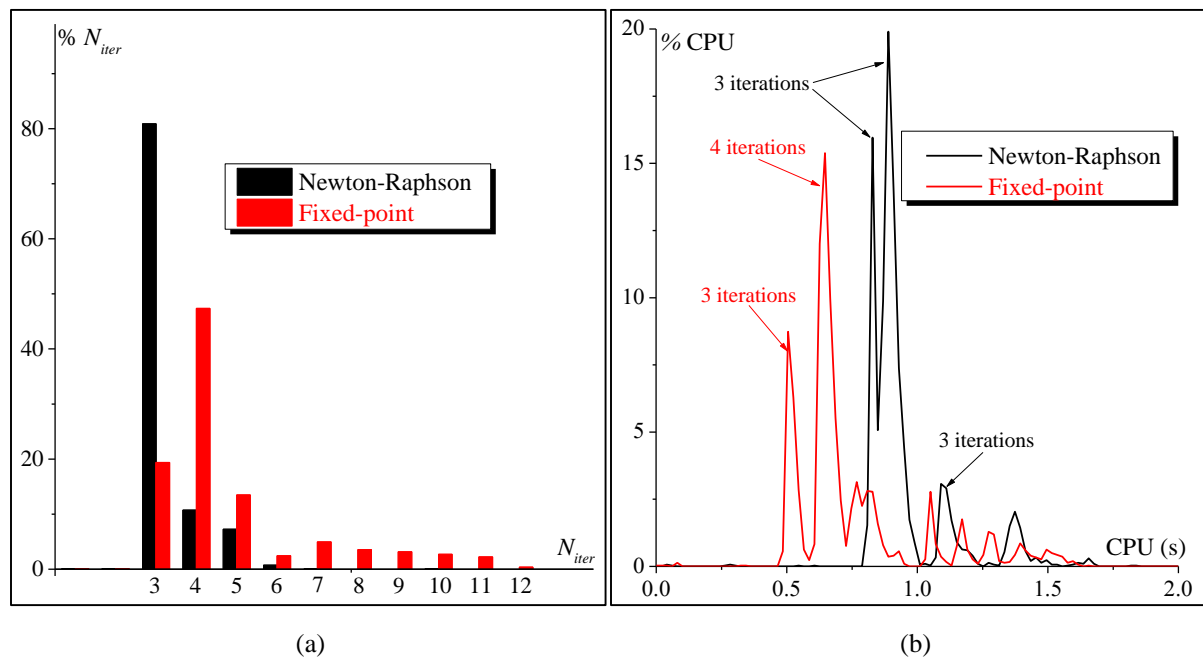
Fig. 16. Comparison between the efficiency of the Newton–Raphson scheme and the fixed-point method in solving the self-consistent equations: (a) Statistical distribution of the number of iterations; (b) Statistical distribution of the CPU time.

4.4. Structural simulations

In order to assess the capability of the developed algorithms of simulating more complex structural components subject to more complex loading paths, a circular deep-drawing process is simulated by using ABAQUS/Standard FE code and the UMATs developed in this work. The description of the tool set-up is shown in Fig. 17a. The diameter of the punch is taken equal to 33.0 mm. The fillet radii of the punch and of the die in contact with the metal sheet are set to 4.0 mm. Contact between the sheet and the tools is imposed through an isotropic Coulomb friction model with friction coefficient $\eta = 0.17$. The diameter and the thickness of the sheet are set to 74.0 mm and 1.0 mm, respectively. The die, punch, and blank holder are modeled as analytical rigid surfaces and are meshed by 5182, 2850, and 1012 C3D4 rigid shell elements, respectively. As to the specimen, it is discretized with 1276 eight-node hexahedral reduced-integration solid finite elements C3D8R, taken from ABAQUS elements library, as shown in Fig. 17b (with two element layers through the thickness). The size of the smallest element in the mesh is set to 1.0 mm. A polycrystalline aggregate made of 200 grains is associated with each integration point of the sheet mesh. Thus, the specimen is made of $1276 \times 200 = 255200$ grains. The initial crystallographic orientations and volume fractions of the different grains are randomly distributed. As shown in Fig. 17b, the mesh density is increased in the contact zone between the punch and the specimen. One computation is performed for each of the developed polycrystalline UMATs: based on the DCSC, DRSC and DCRSC algorithms.
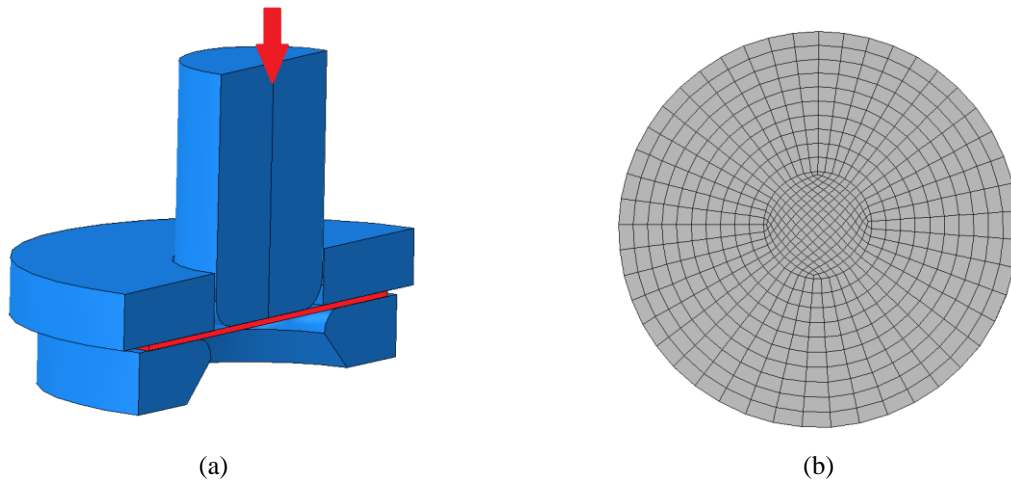
(a)   (b)

Fig. 17. Circular cup deep-drawing simulation: (a) Schematic description of the tools (in blue) and the circular sheet (in red); (b) Mesh of the sheet.

To carry out the forming process, the punch moves in the vertical direction until the final targeted depth, or until the FE computations no longer converge. The final shape of the sheet, obtained by the DCRSC algorithm, is shown in Fig. 18a. At this moment, the vertical displacement U is equal to 5.8 mm. The DCSC and DRSC algorithms both fail to converge, for the reasons detailed in Section 4.3, at different displacement levels, as shown in Fig. 18b. For the DCRSC, convergence failure of the FE computations corresponds to a drastic decrease in the stress level in at least one of the integration points of the mesh. At this moment, final failure is assumed to be reached in the corresponding integration point. As explained later, the DCSC algorithm is the least stable algorithm, while the DRSC scheme fails later when important damage occurs at the grain level. The curves plotted in Fig. 18b show that the different algorithms give close predictions. These results confirm once again the higher performance of the DCRSC algorithm compared to the two other algorithms.
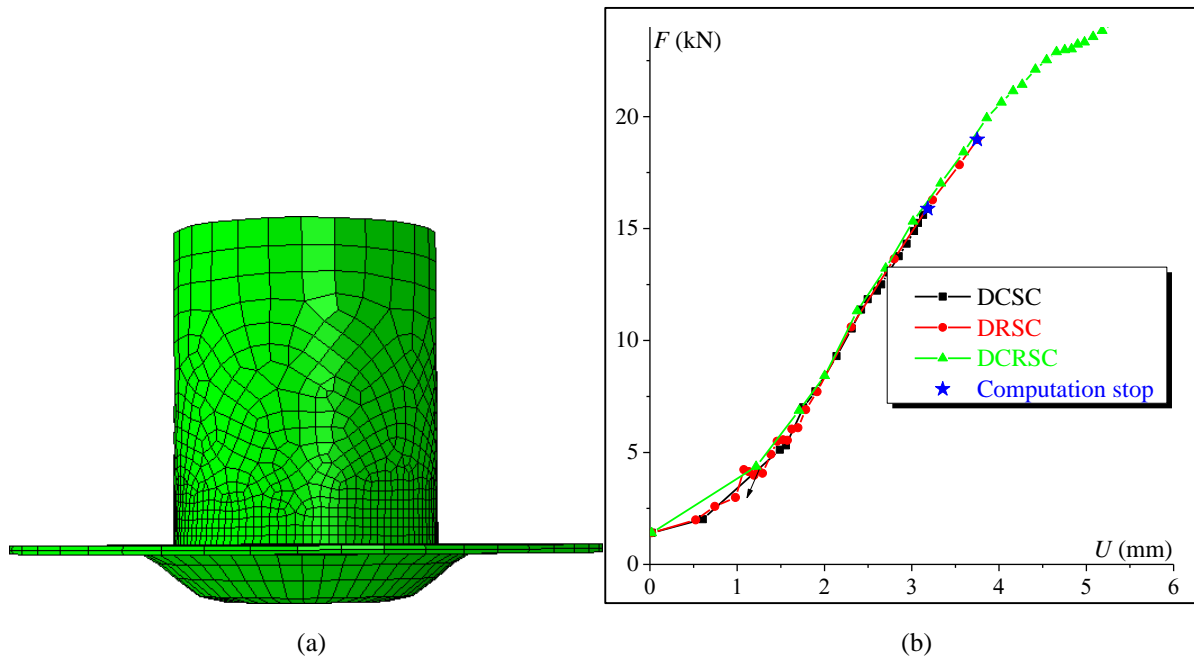
| (a) | (b) |

Fig. 18. Numerical results for the cup-drawing simulations: (a) Final shape of the sheet; (b) Punch force–displacement curves predicted by the different algorithms.

The distribution of the maximum value of the macroscopic logarithmic strain, the macroscopic equivalent stress and the macroscopic damage measure, as predicted by the DCRSC implementation, at the end of the forming process are shown in Fig. 19. Figure 19c reveals that the macroscopic damage distribution not only depends on the strain level (Fig. 19a), but also on the initial anisotropy of the material (which is quite expectable). Furthermore, the softening phenomenon is observed in the region exhibiting the maximum damage level (see the red zone in Fig. 19c), as the stress level is relatively low in this zone (Fig. 19b). It could be noticed also that the values of the macroscopic damage measure D^{poly} do not exceed 0.06, despite the fact that final failure is reached in a narrow zone of the sheet. This latter observation is consistent with the results presented in Fig. 12a and b.
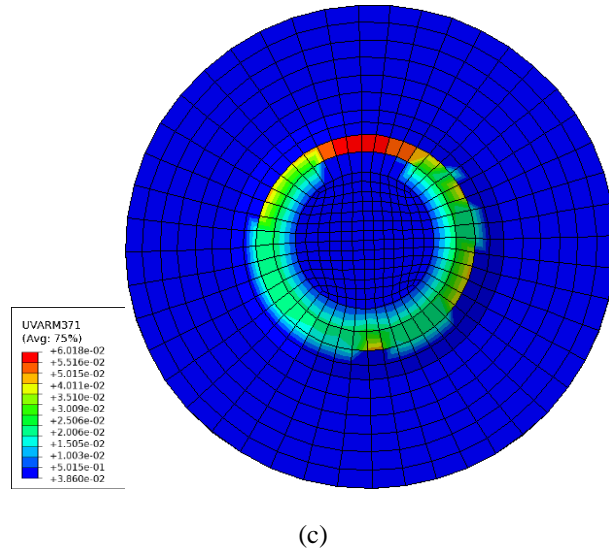

| (a) | (b) |

-47-

(c)
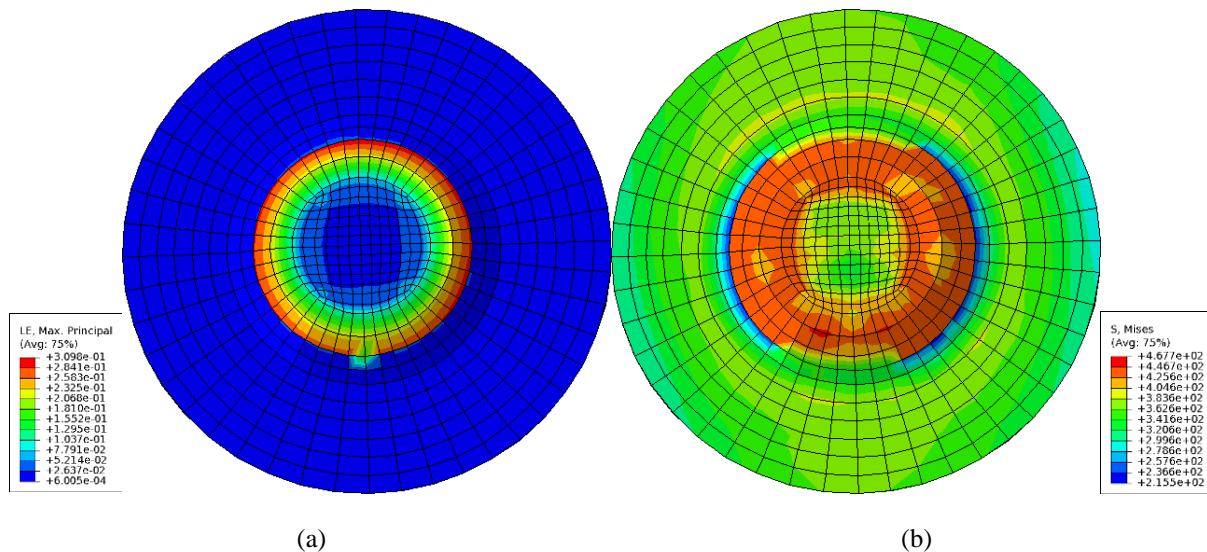
Fig. 19. Macroscopic results: (a) Contour plot of the maximum logarithmic strain LE_{max} ; (b) Contour plot of the equivalent stress Σ_{eq} ; (c) Contour plot of the macroscopic damage measure D^{poly} .

5. Conclusions

A finite strain elasto-plastic self-consistent model for damaged polycrystalline aggregates has been proposed and implemented into ABAQUS/Standard FE code. To model the coupling between damage phenomena and single crystal elasto-plasticity, a damage variable has been introduced at each CSS for each individual grain. The single crystal plastic flow is modeled by both the classical (DCSC) and a regularized (DRSC) version of the Schmid criterion. Two efficient and robust numerical algorithms have been developed and implemented to integrate the constitutive equations corresponding to the two single crystal models. The single crystal simulations demonstrate that the DCSC algorithm has significantly higher performance than the DRSC one (CPU time, convergence of the iterative computation). However, the coupling of the DCSC algorithm with the self-consistent scheme leads to severe convergence issues caused by the persistent evolution of the CSS activation, inducing abrupt changes in the components of the microscopic tangent moduli. This problem is obviously avoided when the DRSC algorithm is used, as all the CSSs are simultaneously activated. Hence, to improve the performance of the self-consistent computations and to avoid the above numerical problems, a new numerical scheme has been built. This scheme, shortly named DCRSC, allows combining the benefits of the two schemes: the DCSC is used to integrate the single crystal constitutive equations, while the DRSC is used to compute the microscopic tangent moduli required for solving the self-consistent equations. The presented numerical predictions highlight the high performance of the DCRSC algorithm, compared to the DCSC and DRSC algorithms, in the prediction of the mechanical behavior of polycrystalline aggregates as well as in the simulation of a more complex forming process. Then, this optimized algorithm will be used in several future investigations to simulate various working processes, such as stamping and single point forming

processes. These investigations will enable to explicitly link microstructural relevant phenomena and the interaction between them (residual stresses, grain strain heterogeneity, texture evolution, microscopic damage) to the macroscopic ductility of formed components. Such information cannot be easily obtained by classical phenomenological models.

Acknowledgment

Appendix A. Kinematics of finite strain crystal plasticity

In what follows, we briefly describe the single crystal kinematics at finite strains. As a starting point, the microscopic velocity gradient $\mathbf{g}$ is expressed in terms of the microscopic deformation gradient $\mathbf{f}$ according to:

$$\mathbf{g} = \dot{\mathbf{f}}.\mathbf{f}^{-1}. \tag{A.1}$$

The deformation gradient $\mathbf{f}$ can be multiplicatively decomposed into an elastic part $\mathbf{f}^e$ and a plastic part $\mathbf{f}^p$ (Fig. A.1):

$$\mathbf{f} = \mathbf{f}^e.\mathbf{f}^p. \tag{A.2}$$

The elastic part $\mathbf{f}^e$ may, itself, be decomposed into a symmetric stretching tensor $\mathbf{v}^e$ and a rotation $\mathbf{r}^e$ defining the orientation of the coordinate system associated with the intermediate configuration relative to its counterpart in the current one:

$$\mathbf{f}^e = \mathbf{v}^e.\mathbf{r}^e. \tag{A.3}$$

The substitution of Eqs. (A.2) and (A.3) into Eq. (A.1) yields:

$$
\begin{aligned}
\mathbf{g} &= \dot{\mathbf{f}}.\mathbf{f}^{-1} = \dot{\mathbf{f}}^e.\mathbf{f}^{e-1} + \mathbf{f}^e.\dot{\mathbf{f}}^p.\mathbf{f}^{p-1}.\mathbf{f}^{e-1} \\
&= \dot{\mathbf{v}}^e.\mathbf{v}^{e-1} + \mathbf{v}^e.\dot{\mathbf{r}}^e.\mathbf{r}^{eT}.\mathbf{v}^{e-1} + \mathbf{v}^e.\mathbf{r}^e.\dot{\mathbf{f}}^p.\mathbf{f}^{p-1}.\mathbf{r}^{eT}.\mathbf{v}^{e-1}.
\end{aligned}
\tag{A.4}
$$

Since the elastic deformation remains very small compared to the unity, for metallic materials, the stretching tensor $\mathbf{v}^e$ can be approximated by the second-rank identity tensor ($\mathbf{v}^e \approx \mathbf{I}_2$). Under this approximation, Eq. (A.4) can be simplified in the following form:

$$\mathbf{g} = \dot{\mathbf{v}}^{e-1} + \dot{\mathbf{r}}^e.\mathbf{r}^{eT} + \mathbf{r}^e.\dot{\mathbf{f}}^p.\mathbf{f}^{p-1}.\mathbf{r}^{eT}. \tag{A.5}$$

The velocity gradient $\mathbf{g}$ can be decomposed into symmetric, $\mathbf{d}$, and antisymmetric, $\mathbf{w}$, parts as:

$$\mathbf{d} = \frac{1}{2}\left(\mathbf{g} + \mathbf{g}^T\right) \quad ; \quad \mathbf{w} = \frac{1}{2}\left(\mathbf{g} - \mathbf{g}^T\right), \tag{A.6}$$

which can be additively split into elastic and plastic contributions:

$$\mathbf{d} = \mathbf{d}^e + \mathbf{d}^p \quad ; \quad \mathbf{w} = \mathbf{w}^e + \mathbf{w}^p, \tag{A.7}$$

with:

$$\mathbf{d}^e = \dot{\mathbf{v}}^{e-1} \quad ; \quad \mathbf{w}^e = \dot{\mathbf{r}}^e . \mathbf{r}^{eT}$$

$$\mathbf{d}^p = \frac{1}{2} \mathbf{r}^e . \left(\dot{\mathbf{f}}^p . \mathbf{f}^{p-1} + \left(\dot{\mathbf{f}}^p . \mathbf{f}^{p-1} \right)^T \right) . \mathbf{r}^{eT} \quad ; \quad \mathbf{w}^p = \frac{1}{2} \mathbf{r}^e . \left(\dot{\mathbf{f}}^p . \mathbf{f}^{p-1} - \left(\dot{\mathbf{f}}^p . \mathbf{f}^{p-1} \right)^T \right) . \mathbf{r}^{eT}. \tag{A.8}$$
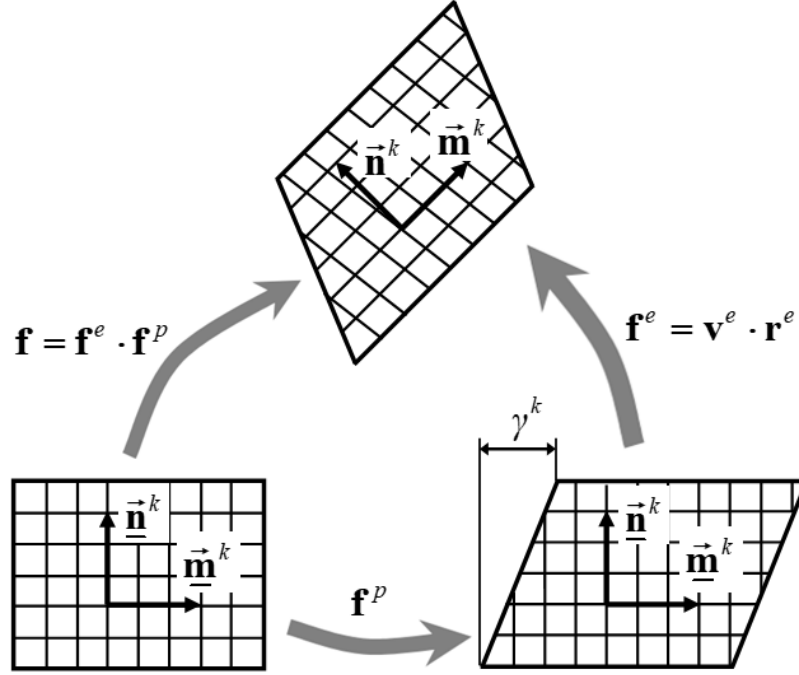

Fig. A.1. Schematic representation of the multiplicative decomposition of the deformation gradient: plastic slip and rigid rotation along with elastic distortion of the crystallographic lattice.

Appendix B. Computation of tensor $\mathbf{Y}^k$

The computation of the second-rank tensor $\mathbf{Y}^k$ depends on the adopted plastic flow rule.

B.1. DCSC

To obtain the incremental expression of tensor $\mathbf{Y}^k$ for the DCSC scheme, the following relationship between B^k given in Eq. (76)₃ and $\mathbf{g}$ can be established:

$$\forall k \in \mathcal{A}: \quad B^k = -\mathbf{M} : \mathbf{g} : \widehat{\boldsymbol{\mu}}_c^k, \tag{B.1}$$

where $\mathbf{M}$ is a symmetric fourth-rank tensor defined such that:

$$\mathbf{M} : \mathbf{g} = \tilde{\mathbf{c}}^e : \mathbf{d}. \tag{B.2}$$

When matrix $\mathbf{A}$ (Eq. (84)) is invertible, the slip rates of the active CSSs are solution of Eq. (75). Performing a first-order Taylor expansion of $\dot{\tilde{\gamma}}^k$ in the form:

$$\forall k \in \mathcal{A}: \quad \dot{\tilde{\gamma}}^k = \mathbf{Y}^k : \mathbf{g} + o\left(\|\mathbf{g}\|_2\right), \tag{B.3}$$

and combining Eqs. (75), (B.1) and (B.3), one can show that:

$$\forall k \in \mathcal{A}: \quad \dot{\tilde{\gamma}}^k = \widehat{A}^{kl} \mathbf{M} : \mathbf{g} : \widehat{\boldsymbol{\mu}}_c^l + o\left(\|\mathbf{g}\|_2\right) \quad ; \quad l \in \mathcal{A}. \tag{B.4}$$

The comparison between Eqs. (45) and (B.4) allows us to identify the expression of tensor $\mathbf{Y}^k$:

$$\forall k \in \mathcal{A}: \quad \mathbf{Y}^k = \widehat{A}^{kl} \widehat{\boldsymbol{\mu}}_c^l : \mathbf{M} \quad ; \quad l \in \mathcal{A}. \tag{B.5}$$

B.2. DRSC

To determine the expression of tensor $\mathbf{Y}^k$, required for the computation of the analytical tangent modulus, the expression of the plastic multiplier $\dot{\lambda}$ should be derived from the consistency condition:

$$\dot{\tilde{f}}_{reg} = \frac{\mathrm{d}}{\mathrm{d}t}\left[\sum_{k=1}^{N_s}\left(\frac{\widehat{\tilde{\tau}}^k}{\tau_c^k}\right)^{2n}\right] = 0. \tag{B.6}$$

By using Eqs. (16) and (20), Eq. (B.6) can be expressed as:

$$\dot{\tilde{f}}_{reg} = 2n\sum_{k=1}^{N_s}\left(\dot{\boldsymbol{\sigma}}^c : \frac{\widehat{\boldsymbol{\mu}}_c^k}{\tau_c^k\sqrt{1-d^k}} - \dot{d}^k \boldsymbol{\sigma} : \frac{\widehat{\boldsymbol{\mu}}_c^k}{2\left(1-d^k\right)^{3/2}\tau_c^k} + \frac{\alpha\tilde{\sigma}_\eta^k\sum_{r=1}^{2N_s}\dot{d}^r}{\tau_c^k} - \dot{\tau}_c^k\frac{\widehat{\tilde{\tau}}^k}{\left(\tau_c^k\right)^2}\right)\left(\frac{\widehat{\tilde{\tau}}^k}{\tau_c^k}\right)^{2n-1}, \tag{B.7}$$

where

$$\forall \, k = 1,...,N_s: \quad \dot{d}^k = \dot{\lambda}\left(\kappa^k + \kappa^{k+N_s}\right)v^k \quad ; \quad \dot{\tau}_c^k = \dot{\lambda}\, h^{kl}\kappa^l \quad ; \quad l = 1,...,2N_s. \tag{B.8}$$

The substitution of Eqs. (B.8) into Eq. (B.7) allows us to rewrite the expression of $\dot{\tilde{f}}_{reg}$ as:

$$\dot{\tilde{f}}_{reg} = 2n\sum_{k=1}^{N_s}\left(\dot{\boldsymbol{\sigma}}^c : \frac{\widehat{\boldsymbol{\mu}}_c^k}{\tau_c^k\sqrt{1-d^k}} - \dot{\lambda}\left(\kappa^k + \kappa^{k+N_s}\right)v^k\boldsymbol{\sigma} : \frac{\widehat{\boldsymbol{\mu}}_c^k}{2\left(1-d^k\right)^{3/2}\tau_c^k} + \frac{2\alpha\tilde{\sigma}_\eta^k\sum_{r=1}^{2N_s}\dot{\lambda}\kappa^r v^r}{\tau_c^k} - \dot{\lambda}\, h^{kl}\kappa^l\frac{\widehat{\tilde{\tau}}^k}{\left(\tau_c^k\right)^2}\right)\left(\frac{\widehat{\tilde{\tau}}}{\tau_c^k}\right)^{2n-1}. \tag{B.9}$$

To simplify the following developments, let us introduce $\dot{\boldsymbol{\sigma}}^{\dot{\lambda}}$ defined as:

$$\dot{\boldsymbol{\sigma}}^{\dot{\lambda}} = \kappa^k\left(\frac{1}{N_s}v^k\mathbf{c}^e : \boldsymbol{\varepsilon}^e + \frac{\tilde{\mathbf{c}}^e : \widehat{\boldsymbol{\mu}}_{d^p}^k}{\sqrt{1-d^k}}\right) \quad ; \quad k = 1,...,2N_s. \tag{B.10}$$

Using this definition, Eq. (72) defining the corotational stress rate $\dot{\boldsymbol{\sigma}}^c$ can be rewritten as:

$$\dot{\boldsymbol{\sigma}}^c = \tilde{\mathbf{c}}^e : \mathbf{d} - \dot{\lambda}\dot{\boldsymbol{\sigma}}^{\dot{\lambda}}. \tag{B.11}$$

The insertion of expression (B.11) of $\dot{\boldsymbol{\sigma}}^c$ into the consistency condition (B.9) allows writing this latter in the following generic form:

$$\dot{\tilde{f}}_{reg} = B^{\dot{\lambda}} - \dot{\lambda} A^{\dot{\lambda}} = 0, \tag{B.12}$$

where $A^{\dot{\lambda}}$ and $B^{\dot{\lambda}}$ are given by the following formulas:

$$A^{\dot{\lambda}} = \sum_{k=1}^{N_s} \left(-\dot{\boldsymbol{\sigma}}^{\dot{\lambda}} : \frac{\widehat{\boldsymbol{\mu}}_c^k}{\sqrt{1-d^k}\,\tau_c^k} - (\kappa^k + \kappa^{k+N_s})\upsilon^k \boldsymbol{\sigma} : \frac{\widehat{\boldsymbol{\mu}}_c^k}{2\left(1-d^k\right)^{3/2}\tau_c^k} + \frac{2\alpha\tilde{\sigma}_\eta^k \sum_{r=1}^{2N_s}\kappa^r\upsilon^r}{\tau_c^k} - h^{kl}\kappa^l \frac{\widehat{\tilde{\tau}}^k}{\left(\tau_c^k\right)^2} \right) \left(\frac{\widehat{\tilde{\tau}}^k}{\tau_c^k} \right)^{2n-1};$$

$$B^{\dot{\lambda}} = -\tilde{\mathbf{c}}^e : \mathbf{d} : \sum_{k=1}^{N_s} \frac{\widehat{\boldsymbol{\mu}}_c^k}{\sqrt{1-d^k}\,\tau_c^k} \left(\frac{\widehat{\tilde{\tau}}^k}{\tau_c^k} \right)^{2n-1}.$$

(B.13)

Finally, the plastic multiplier $\dot{\lambda}$ can be deduced from Eq. (B.12):

$$\dot{\lambda} = \frac{B^{\dot{\lambda}}}{A^{\dot{\lambda}}}. \tag{B.14}$$

To derive the expression of tensor $\mathbf{Y}^k$ for the DRSC, scalar $B^{\dot{\lambda}}$ defined by Eq. (B.13)$_2$ should be expressed as a function of the Eulerian velocity gradient $\mathbf{g}$ as follows:

$$B^{\dot{\lambda}} = -\mathbf{M} : \mathbf{g} : \sum_{k=1}^{N_s} \frac{\widehat{\boldsymbol{\mu}}_c^k}{\sqrt{1-d^k}\,\tau_c^k} \left(\frac{\widehat{\tilde{\tau}}^k}{\tau_c^k} \right)^{2n-1}, \tag{B.15}$$

where the fourth-rank tensor $\mathbf{M}$ has the same definition as that given in Eq. (B.2). Then, tensor $\mathbf{Y}^k$ can be deduced by combining Eqs. (A.5), (35) and (B.15):

$$\mathbf{Y}^k = -\frac{\kappa^k}{A^{\dot{\lambda}}} \sum_{l=1}^{N_s} \frac{\widehat{\boldsymbol{\mu}}_c^l}{\sqrt{1-d^l}\,\tau_c^l} \left(\frac{\widehat{\tilde{\tau}}^l}{\tau_c^l} \right)^{2n-1} : \mathbf{M}. \tag{B.16}$$

Appendix C. Solving the self-consistent equations by the Newton–Raphson scheme

C.1. Iterative Newton–Raphson algorithm

The Newton–Raphson scheme consists in reducing to zero an error function using a Taylor expansion of order 1. Here, the error function is:

$$\mathbf{Err}(\mathcal{L}) = \mathcal{L} - \sum_{gr=1}^{Ngr} f^{gr} \boldsymbol{\ell}^{gr} : \mathbf{A}^{gr}. \tag{C.1}$$

The Taylor expansion reads:

$$\mathbf{Err}(\mathcal{L} + d\mathcal{L}) = \mathbf{Err}(\mathcal{L}) + \nabla\mathbf{Err}(\mathcal{L}).d\mathcal{L}. \tag{C.2}$$

The expression of the Jacobian matrix $\nabla\mathbf{Err}(\mathcal{L})$ can be derived after some lengthy computations

summarized in Section C.2. The Newton–Raphson algorithm used to solve the non-linear system (C.1) is summarized by the following steps:

- *Step 0*: set the first guess for the macroscopic tangent modulus $\mathcal{L}^{(0)}$ and the tangent moduli $\ell^{gr\,(0)}$ to their converged values at the previous increment.

- *Step 1*: for $i \geq 1$, compute the interaction tensor $\mathbf{T}^{gr\,(i)}$, the localization tensor $\mathbf{A}^{gr\,(i)}$, the microscopic velocity gradient $\mathbf{g}^{gr\,(i)}$ and the microscopic tangent moduli $\ell^{gr\,(i)}$ as in *Step 1* of the fixed-point algorithm (Section 3.2).

- *Step 2*: compute the error vector:

$$\mathbf{Err}\left(\mathcal{L}^{(i)}\right) = \mathcal{L}^{(i)} - \sum_{gr=1}^{Ngr} f^{gr}\, \ell^{gr\,(i)} : \mathbf{A}^{gr\,(i)}, \tag{C.3}$$

and the associated Jacobian matrix $\nabla\mathbf{Err}\left(\mathcal{L}^{(i)}\right)$. If $\left(\left\|\mathbf{Err}\left(\mathcal{L}^{(i)}\right)\right\| / \left\|\mathcal{L}^{(i)}\right\|\right) < 10^{-6}$, then the convergence of the self-consistent scheme is reached. Else, go to *Step 3*.

- *Step 3*: compute the new iteration $\mathcal{L}^{(i+1)}$ as follows:

$$d\mathcal{L}^{(i+1)} = \left(\nabla\mathbf{Err}\left(\mathcal{L}^{(i)}\right)\right)^{-1}.\mathbf{Err}\left(\mathcal{L}^{(i)}\right) \quad ; \quad \mathcal{L}^{(i+1)} = \mathcal{L}^{(i)} + d\mathcal{L}^{(i+1)}. \tag{C.4}$$

- *Step 4*: set $i = i + 1$ and go to *Step 1*.

As in the fixed-point algorithm, Eq. (63) is used to update the grain volume fraction.

C.2. Computation of the Jacobian matrix

The error function defined by Eq. (C.1) is expanded by introducing the complete form of the localization tensor $\mathbf{A}^{gr}$ given by Eq. (8):

$$\mathbf{Err}\left(\mathcal{L}\right) = \mathcal{L} - \sum_{gr=1}^{Ngr} f^{gr}\, \ell^{gr} : \left(\mathbf{I}_4 - \mathbf{T}^{gr} : \left(\ell^{gr} - \mathcal{L}\right)\right)^{-1} : \left(\sum_{gr=1}^{Ngr} f^{gr} \left(\mathbf{I}_4 - \mathbf{T}^{gr} : \left(\ell^{gr} - \mathcal{L}\right)\right)^{-1}\right)^{-1}. \tag{C.5}$$

To perform the differentiation of (C.5) with respect to $\mathcal{L}$, we recall the derivative of the inverse of a matrix $\mathbf{M}$:

$$\frac{\partial \mathbf{M}^{-1}}{\partial \mathcal{L}} = -\mathbf{M}^{-1}.\frac{\partial \mathbf{M}}{\partial \mathcal{L}}.\mathbf{M}^{-1}. \tag{C.6}$$

To simplify the subsequent developments, let us introduce tensors $\mathbf{B}^{gr}$ and $\mathbf{C}^{gr}$ defined as:

$$\mathbf{B}^{gr} = \mathbf{I}_4 - \mathbf{T}^{gr} : \left(\ell^{gr} - \mathcal{L}\right) \quad ; \quad \mathbf{C}^{gr} = \sum_{gr=1}^{Ngr} f^{gr} \left(\mathbf{B}^{gr}\right)^{-1}. \tag{C.7}$$

Owing to the explicit integration of the single crystal constitutive equations for both versions of the Schmid flow rule, the dependence of the microscopic tangent modulus ℓ^{gr} on the microscopic velocity

gradient $\mathbf{g}^{gr}$ and then on the macroscopic tangent modulus $\mathcal{L}$ remains very weak (except in the case of an abrupt change in the activity of CSSs, sometimes observed when the DCSC is used). Thus, the derivative $\partial\ell^{gr}/\partial\mathcal{L}$ may be reasonably neglected in the computation of the gradient operator used in the Newton–Raphson scheme. Hence, the derivatives of tensors $\mathbf{B}^{gr}$ and $\mathbf{C}^{gr}$ with respect to $\mathcal{L}$ can be computed as:

$$\forall gr: \quad \frac{\partial\mathbf{B}^{gr}}{\partial\mathcal{L}} = -\frac{\partial\mathbf{T}^{gr}}{\partial\mathcal{L}} : \left(\ell^{gr} - \mathcal{L}\right) + \mathbf{T}^{gr} : \mathbf{I}_8 ; \tag{C.8}$$

$$\forall gr: \quad \frac{\partial\mathbf{C}^{gr}}{\partial\mathcal{L}} = -\sum_{gr=1}^{Ngr} f^{gr} \left(\mathbf{B}^{gr}\right)^{-1} . \frac{\partial\mathbf{B}^{gr}}{\partial\mathcal{L}} . \left(\mathbf{B}^{gr}\right)^{-1} , \tag{C.9}$$

where $\partial\mathbf{T}^{gr}/\partial\mathcal{L}$ is evaluated numerically. Finally, equations (C.5), (C.6), (C.8) and (C.9) lead to the following expression of the Jacobian matrix:

$$\nabla\mathbf{Err} = \mathbf{I}_8 + \sum_{gr=1}^{Ngr} f^{gr} \ell^{gr} : \left(\mathbf{B}^{gr}\right)^{-1} . \frac{\partial\mathbf{B}^{gr}}{\partial\mathcal{L}} . \left(\mathbf{B}^{gr}\right)^{-1} : \left(\mathbf{C}^{gr}\right)^{-1} + f^{gr} \ell^{gr} : \mathbf{B}^{gr} : \left(\mathbf{C}^{gr}\right)^{-1} . \frac{\partial\mathbf{C}^{gr}}{\partial\mathcal{L}} . \left(\mathbf{C}^{gr}\right)^{-1} , \tag{C.10}$$

with $\mathbf{I}_8$ the eighth-rank identity tensor.

References

[1] J. Bauschinger, Über die veränderung der elastizitätsgrenze und der festigkeit des eisens und stahls durch strecken und quetschen, durch erwärmen und abkühlen und durch oftmals wiederholte beanspruchung, Mitt. Mech.-Tech. Lab. Münch. 13 (1) (1886) 1836–1877.

[2] S. Ghorbanpour, M. Zecevic, A. Kumar, M. Jahedi, J. Bicknell, L. Jorgensen, I.J. Beyerlein, M. Knezevic, A crystal plasticity model incorporating the effects of precipitates in superalloys: application to tensile, compressive, and cyclic deformation of inconel 718, Int. J. Plast. 99 (2017) 162–185.

[3] S. Gribbin, J. Bicknell, L. Jorgensen, I. Tsukrov, M. Knezevic, Low cycle fatigue behavior of direct metal laser sintered inconel alloy 718, Int. J. Fatigue 93 (2016) 156–167.

[4] M. Knezevic, I.J. Beyerlein, D.W. Brown, T.A. Sisneros, C.N. Tomé, A polycrystal plasticity model for predicting mechanical response and texture evolution during strain-path changes: application to beryllium, Int. J. Plast. 49 (2013) 185–198.

[5] E.J. Pavlina, M.-G. Lee, F. Barlat, Observations on the nonlinear unloading behavior of advanced high strength steels, Metall. Mater. Trans. A 46 (1) (2015) 18–22.

[6] T.J. Barrett, M. Knezevic, Deep drawing simulations using the finite element method embedding a multi-level crystal plasticity constitutive law: experimental verification and sensitivity analysis, Comput. Methods in Appl. Mech. Eng. 354 (2019) 245–270.

[7] M. Zecevic, W. Pantleon, R.A. Lebensohn, R.J. McCabe, M. Knezevic, Predicting intragranular misorientation distributions in polycrystalline metals using the viscoplastic self-consistent formulation, Acta Mater. 140 (2017) 398–410.

[8] O. Cazacu, B. Revil-Baudard, On the effect of the matrix tension–compression asymmetry on damage evolution in porous plastic solids, Eur. J. Mech. A-Solids 37 (2016)35–44.

[9] O. Cazacu, B. Revil-Baudard, N. Chandola, Plasticity-Damage Couplings: From Single Crystal to Polycrystalline Materials, Springer (2018).

[10] G.I. Taylor, C.F. Elam, Bakerian lecture: the distortion of an aluminium crystal during a tensile test, Proc. Roy. Soc. A 102 (719) (1923) 643–667.

[11] J. Mandel, Généralisation de la théorie de plasticité de W.T. Koiter, Int. J. Solids Struct. 1 (1965) 273–295.

[12] R. Hill, J. Rice, Constitutive analysis of elastic-plastic crystals at arbitrary strain, J. Mech. Phys. Solids 20 (6) (1972) 401–413.

[13] R.J. Asaro, Crystal plasticity, J. Appl. Mech.-Trans. 50 (4b) (1983) 921–934.

[14] E. Schmid, W. Boas, Kristallplastizität, Springer (1935).

[15] W. Gambin, F. Barlat, Modeling of deformation texture development based on rate independent crystal plasticity, Int. J. Plast. 13 (1-2) (1997) 75–85.

[16] A. Abdul-Latif, K. Saanouni, Damaged anelastic behavior of FCC polycrystalline metals with micromechanical approach, Int. J. Damage. Mech. 3 (3) (1994) 237–259.

[17] K. Saanouni, A. Abdul-Latif, Micromechanical modeling of low cycle fatigue under complex loadings - part I. Theoretical formulation, Int. J. Plast. 12 (9) (1996) 1111–1121.

[18] L. Anand, M. Kothari, A computational procedure for rate-independent crystal plasticity, J. Mech. Phys. Solids 44 (4) (1996) 525–558.

[19] C. Miehe, J. Schröder, A comparative study of stress update algorithms for rate-independent and rate-dependent crystal plasticity, Int. J. Numer. Meth. Eng. 5 (2001) 273–298.

[20] A. Cuitiño, M. Ortiz, Computational modelling of single crystals, Model. Simul. Mater. B-Solid 36 (1993) 3815–3840.

[21] M. Schmidt-Baldassari, Numerical concepts for rate-independent single crystal plasticity, Comput. Methods in Appl. Mech. Eng. 192 (11-12) (2003) 1261–1280.

[22] R.I. Borja, J.R. Wren, Discrete micromechanics of elastoplastic crystals, Int. J. Numer. Meth. Eng. 36 (22) (1993) 3815–3840.

[23] R. Knockaert, Y. Chastel, E. Massoni, Rate-independent crystalline and polycrystalline plasticity, application to FCC materials, Int. J. Plast. 16 (2) (2000) 179–198.

[24] R. McGinty, D. McDowell, A semi-implicit integration scheme for rate independent finite crystal plasticity, Int. J. Plast. 22 (6) (2006) 996–1025.

[25] M. Ben Bettaieb, Modélisation du comportement des matériaux polycristallins par homogénéisation périodique, Ph.D. thesis, Aix-Marseille 2 (2006).

[26] M. Ben Bettaieb, O. Débordes, A. Dogui, L. Duchêne, C. Keller, On the numerical integration of rate independent single crystal behavior at large strain, Int. J. Plast. 32–33 (2012) 184–217.

[27] H.K. Akpama, M. Ben Bettaieb, F. Abed-Meraim, Numerical integration of rate-independent BCC single crystal plasticity models: Comparative study of two classes of numerical algorithms, Int. J. Numer. Meth. Eng. 108 (5) (2016) 363–422.

[28] H.K. Akpama, M. Ben Bettaieb, F. Abed-Meraim, Influence of the yield surface curvature on the forming limit diagrams predicted by crystal plasticity theory, Lat. Am. J. Solids Stru. 13 (12) (2016) 2231–2250.

[29] M. Knezevic, M. Zecevic, I.J. Beyerlein, R.A. Lebensohn, A numerical procedure enabling accurate descriptions of strain rate-sensitive flow of polycrystals within crystal visco-plasticity theory, Comput. Methods in Appl. Mech. Eng. 308 (2016) 468–482.

[30] M. Zecevic, I.J. Beyerlein, R.J. McCabe, B.A. McWilliams, M. Knezevic, Transitioning rate sensitivities across multiple length scales: Microstructure-property relationships in the Taylor cylinder impact test on zirconium, Int. J. Plast. 84 (2016) 138–159.

[31] M. Knezevic, S.R. Kalidindi, D. Fullwood, Computationally efficient database and spectral interpolation for fully plastic Taylor-type crystal plasticity calculations of face-centered cubic polycrystals, Int. J. Plast. 24 (7) (2008) 1264–1276.

[32] M. Knezevic, H.F. Al-Harbi, S.R. Kalidindi, Crystal plasticity simulations using discrete fourier transforms, Acta Mater. 57 (6) (2009) 1777–1784.

[33] A. Gupta, M. Ben Bettaieb, F. Abed-Meraim, S.R. Kalidindi, Computationally efficient predictions of crystal plasticity based forming limit diagrams using a spectral database, Int. J. Plast. 103 (2018) 168–187.

[34] V. Kouznetsova, M.G. Geers, W. Brekelmans, Multi-scale second-order computational homogenization of multi-phase materials: a nested finite element solution strategy, Comput. Methods in Appl. Mech. Eng. 193 (48-51) (2004) 5525–5550.

[35] T. Otsuka, R. Brenner, B. Bacroix, FFT-based modelling of transformation plasticity in polycrystalline materials during diffusive phase transformation, Int. J. Eng. Sci. 127 (2018) 92–113.

[36] J. Segurado, R.A. Lebensohn, J. LLorca, C.N. Tomé, Multiscale modeling of plasticity based on embedding the viscoplastic self-consistent formulation in implicit finite elements, Int. J. Plast. 28 (1) (2012) 124–140.

[37] M. Zecevic, M. Knezevic, A new visco-plastic self-consistent formulation implicit in dislocation-based hardening within implicit finite elements: Application to high strain rate and impact deformation of tantalum, Comput. Methods in Appl. Mech. Eng. 341 (2018) 888–916.

[38] M. Zecevic, M. Knezevic, An implicit formulation of the elasto-plastic self-consistent polycrystal plasticity model and its implementation in implicit finite elements, Mech. Mater. 136 (2019) 13065.

[39] M. Zecevic, I.J. Beyerlein, M. Knezevic, Coupling elasto-plastic self-consistent crystal plasticity and implicit finite elements: Applications to compression, cyclic tension-compression, and bending to large strains, Int. J. Plast. 93 (2017) 187–211.

[40] M. Zecevic, Y.P. Korkolis, T. Kuwabara, M. Knezevic, Dual-phase steel sheets under cyclic tension–compression to large strains: Experiments and crystal plasticity modeling, J. Mech. Phys. Solids 96 (2016) 65–87.

[41] R. Hill, On constitutive macro-variables for heterogeneous solids at finite strain, Proc. Roy. Soc. A 326 (1565) (1972) 131–147.

[42] P. Lipinski, M. Berveiller, Elastoplasticity of micro-inhomogeneous metals at large strains, Int. J. Plast. 5 (1989) 149–172.

[43] P. Lipinski, M. Berveiller, E. Reubrez, J. Morreale, Transition theories of elastic-plastic deformation of metallic polycrystals, Arch. Appl. Mech. 65 (5) (1995) 291–311.

[44] M. Zecevic, M. Knezevic, Latent hardening within the elasto-plastic self-consistent polycrystal homogenization to enable the prediction of anisotropy of AA6022-T4 sheets, Int. J. Plast. 105 (2018) 141–163.

[45] O. Fassi-Fehri, Le problème de la paire d'inclusions plastiques et hétérogènes dans une matrice anisotrope : application à l'étude du comportement des matériaux composites et de la plasticité, Ph.D. thesis, Université Paul Verlaine-Metz (1985).

[46] M. Berveiller, O. Fassi-Fehri, A. Hihi, The problem of two plastic and heterogeneous inclusions in an anisotropic medium, Int. J. Eng. Sci. 25 (6) (1987) 691–709.

[47] B. Panicaud, K. Saanouni, A. Baczmanski, M. François, L. Cauvin, L. Le Joncour, Theoretical modelling of ductile damage in duplex stainless steels – Comparison between two micro-mechanical elasto-plastic approaches, Comp. Mater. Sci. 50 (2011) 1908–1916.

[48] M. Boudifa, K. Saanouni, J.L. Chaboche, A micromechanical model for inelastic ductile damage prediction in polycrystalline metals for metal forming, Int. J. Mech. Sci. 51 (2009) 453–464.

[49] T.J.R. Hughes, J. Winget, Finite rotation effects in numerical integration of rate constitutive equations arising in large-deformation analysis, Int. J. Numer. Meth. Eng. 15 (12) (1980) 1862–1867.

[50] N. Nguyen, A.M. Waas, Nonlinear, finite deformation, finite element analysis, Z. Angew. Math. Phys. 67 (3) (2016) 35.

[51] B. Beausir, J.-J. Fundenberger, Analysis Tools for Electron and X-ray diffraction, ATEX - software, www.atex-software.eu, Université de Lorraine - Metz, 2017.